Modeling the Seasonal Dependence of the Atmospheric Response to Observed El Niños in 1962–76

NGAR-CHEUNG LAU

Geophysical Fluid Dynamics Laboratory/NOAA, Princeton University, Princeton, NJ 08542

(Manuscript received 15 March 1985, in final form 6 June 1985)

ABSTRACT

Two 15-year atmospheric GCM integrations are conducted with the lower boundary over the tropical Pacific being forced by observed month-to-month sea surface temperature (SST) changes during the period 1962–76. A descriptive account is given on selected aspects of the 30-year model climatology, as well as the anomalous model behavior through the life cycles of El Niño–Southern Oscillation (ENSO) episodes centered in the years 1965, 1969 and 1972. These model results are compared with available observations reported in the published literature. Particular attention is devoted to the timing of various simulated meteorological phenomena with respect to the spatially and temporally evolving SST forcing, and to the climatological seasonal cycle.

An assessment is made of the capability of the model to simulate the seasonal dependence of various climatological features relevant to ENSO. The phenomena examined include the flow field and rainfall in different monsoon regions, the planetary scale waves in the extratropics, and the low-level convergence zones in the tropical Pacific Basin.

The evolutionary response of the model atmosphere in a typical ENSO event is examined using time series of selected circulation indices, composite charts and Hovmöller diagrams. As the warm SST anomaly appears in the eastern equatorial Pacific during the boreal spring and subsequently spreads across the ocean basin, a well-defined sequence of meteorological events is evident in the model atmosphere. The most notable atmospheric response over the tropical Pacific Basin includes weakening of the east–west surface pressure gradient and easterly trades, eastward displacement of the South Pacific Convergence Zone, southward displacement of the Intertropical Convergence Zone, above normal precipitation at and east of the date line, and below normal precipitation over the Indonesian Archipelago. The strongest anomalies are simulated in the northern winter following a warming off the Peruvian coast. The model response in this mature stage is characterized by tropospheric warming throughout the entire tropical zone, and by the appearance in the tropical upper troposphere of a pair of Pacific anticyclones straddling the equator. These anticyclonic centers appear as the starting points of well-organized wave trains spanning the midlatitude zones of both hemispheres. The Northern Hemisphere wave pattern in the Pacific–North American sector bears a strong resemblance to that reported in recent observational studies.

The warm Pacific SST anomaly tends to be replaced a year later by a cold anomaly. The polarities of meteorological anomalies simulated during the cold phase of the ENSO cycle are mostly opposite to those occurring during the warm phase.

Time series analysis of different circulation indices, as well as comparison between simulated amplitudes of atmospheric variability in this experiment and in a "control" experiment without any prescription of interannual SST variations, indicate that the impact of equatorial Pacific SST anomalies on the tropical circulation is much greater than that on the flow patterns in middle latitudes. In particular, the temporal variance of 200 mb height in this perturbed SST experiment is larger than the corresponding quantity in the control experiment by a factor of 2–6 over the tropics; whereas the same SST fluctuations are much less effective in enhancing the variability in middle and higher latitudes. Moreover, perturbations in the equatorial Pacific SST are more strongly correlated with circulation changes in the tropical atmosphere than with changes in the extratropics.

1. Introduction

Recent observational studies have demonstrated that the interannual variability of SST in the tropical Pacific has a strong impact on the global atmospheric circulation. Bjerknes (1966, 1969) was among the first investigators to suggest that El Niño episodes developing off the Peruvian coast may be linked to planetary scale circulations in both zonal and meridional planes. The association between SST anomalies in the Pacific and short-term climate changes within the tropical zone was substantiated by Krueger and Gray (1969); Wright (1977); Julian and Chervin (1978); Pan and Oort (1983), and others. These studies indicate that warm and cold water episodes tend to be associated with distinct phases of an east–west "seesaw" in sea level pressure spanning the tropical Indian and Pacific Oceans. The large-scale zonal circulation implied by this seesaw, referred to as the Southern Oscillation by Walker and Bliss (1932), exerts a marked influence on the patterns of surface trade winds, precipitation and upper-level flow in the tropics. In recent years, many investigations on tropical phenomena associated with El Niño–Southern Oscillation (ENSO) were expedited by the

availability of gridded operational analyses covering the tropics (e.g., Arkin, 1982). Use was also made of measurements of outgoing longwave radiation to infer regions of enhanced and suppressed convective activity during ENSO episodes (e.g., Heddinghaus and Krueger, 1981; Lau and Chan, 1983).

The observational evidence presented by Horel and Wallace (1981), van Loon and Madden (1981), van Loon and Rogers (1981), Chen (1982b), and others have further demonstrated that not only do SST anomalies play a significant role in the tropical circulation, they are also associated with characteristic flow patterns in middle and high latitudes. Hence a global perspective is evidently called for while examining the atmospheric response to changing conditions in tropical oceans.

By analyzing surface data collected along various shipping lanes over the equatorial Pacific during the past three decades, Rasmusson and Carpenter (1982) reconstructed the temporal and spatial evolution of various oceanographic and meteorological parameters in the course of a typical ENSO episode. It was shown that the ENSO cycle is characterized by well-defined antecedent, onset, growth, mature and decay phases. These distinct stages of development are perhaps best described in terms of concomitant changes in the atmospheric circulation as the SST anomaly spreads across the central tropical Pacific. Salient circulation changes linked to the evolution of the warm phase of such episodes include:

- gradual reduction in the strength of surface easterly trades over the equator,
- enhancement of low-level convergence and precipitation along the central and eastern equatorial Pacific, and suppression of precipitation over the Indonesian Archipelago, and
- falling sea level pressures over the eastern South Pacific, and rising sea level pressures over the Indonesia–North Australian sector.

Results from empirical studies by Rasmusson and Carpenter (1982), Horel and Wallace (1981) and others also suggest that the timing of different phases in a typical ENSO episode is closely linked to the climatological seasonal cycle. For instance, positive SST anomalies in the 1960s and 1970s first appeared along the South American coasts in the boreal spring, and eventually spread across the tropical Pacific during the following seasons. It is during the latter stage, which coincides with the Northern Hemisphere winter, when strong tropical precipitation anomalies and strong teleconnections with the extratropics occur. A comprehensive understanding of the phenomena associated with ENSO must therefore take into account the continuously changing oceanic conditions as these episodes evolve, and the role of the seasonal cycle in modulating various stages of development.

The rapid expansion of our empirical knowledge of circulation features related to ENSO has stimulated extensive research on large-scale air–sea interaction using numerical models. The large variety of general circulation model (GCM) experiments aimed at simulating the atmospheric response to anomalous SST forcing have been reviewed in a recent article by Shukla and Wallace (1983). These authors have also presented new results on the impact of Pacific SST anomalies on the atmospheric circulation simulated by the GLAS climate model. Findings from a similar experiment using the NCAR community climate model were reported by Blackmon *et al.* (1983). Other model investigations on ENSO were also conducted recently at the Canadian Climate Center (Boer, 1985), the Laboratoire de Météorologie Dynamique (Michaud and Sadourny, 1984) and the U.K. Meteorological Office (Palmer and Mansfield, 1984). Thus far, many of the modeling efforts have been devoted to simulating the stationary atmospheric response to a prescribed SST anomaly which is *temporally fixed.* The spatial patterns of the SST anomaly used in these experiments are either highly idealized or derived from composites of several events at their respective mature phases. Moreover, with the notable exception of the study by Boer (1985), most of these sensitivity studies are based on model integrations of limited durations (typically several months), or conducted in a model environment set at perpetual solstice conditions. In either case, influences of the climatological seasonal cycle have not been fully taken into account.

In light of the substantial empirical evidence described earlier in this section, an attempt is made in the present investigation to relax two restrictions inherent in most previous modeling studies on ENSO. First, the spatial pattern of the tropical Pacific SST forcing imposed at the lower boundary of the model is allowed to change continuously with time, in the same manner as observed during the 15-year period from 1962–76. Second, the model is subjected to external forcings which evolve through complete seasonal cycles. The present numerical experiment hence facilitates a more incisive assessment of the fidelity of GCMs in simulating the global atmospheric circulation at each individual phase of an ENSO episode. Diagnosis of this model run would also shed new light on the seasonal dependence of various meteorological features associated with ENSO. It needs to be demonstrated that the current generation of atmospheric GCMs is capable of simulating a realistic response to perturbed SST conditions before one can proceed with confidence to study the ENSO phenomena using even more sophisticated tools, such as air–sea coupled models. The present study thus represents an intermediate step in our quest for a full understanding of the highly interactive processes taking place during ENSO.

Some preliminary results from this study have been presented in Lau and Oort (1985), in which global teleconnection patterns and time series depicting the

temporal correlation of the simulated pressure and zonal wind fields with the prescribed SST forcing in the tropical Pacific were compared with observations. Barnett (1985) has also examined the low-frequency variability of the sea level pressure field in this experiment using complex empirical orthogonal functions. Much of the present article is devoted to a phenomenological description of the anomalous model behavior in different stages of an ENSO cycle. By comparing the statistics for this sensitivity experiment with those derived from a run with no SST anomalies imposed, an assessment is also made of the impact of tropical Pacific SST changes on the amplitude and spatial modes of atmospheric variability in different geographical regions.

A brief outline of the experimental design of this study is given in Section 2. The long-term model climatology and its seasonal dependence is examined in Section 3. Time series of selected circulation indices depicting various aspects of anomalous model behavior are displayed in Section 4. Global patterns of the simulated precipitation, geopotential height, horizontal wind vector and streamfunction fields in selected phases of an ENSO life cycle are displayed in Section 5. The temporal evolution of various circulation features appearing in the model atmosphere is further illustrated using Hovmöller diagrams in Section 6. The impact of SST fluctuations in the tropical Pacific on atmospheric variability in the tropics and extratropics is discussed in Section 7, followed by some concluding remarks in Section 8.

2. Experimental design

The global atmospheric GCM used in the present study has been developed at GFDL, and is basically similar to the version described by Manabe *et al.* (1979), Manabe and Hahn (1981) and Lau (1981). The same model has been used by Keshavamurty (1982) to investigate the atmospheric response to idealized Pacific SST anomalies during the northern summer. Horizontal variations in the model atmosphere are represented spectrally in terms of spherical harmonics, with rhomboidal truncation at 15 wavenumbers. There are nine sigma levels in the vertical direction. Realistic continent–ocean contrast and orography are incorporated at the lower boundary. The sea surface temperature is prescribed, whereas the surface temperature over land is determined diagnostically assuming zero heat storage in the ground. Essential model physics includes moist convective adjustment, snow–albedo feedback, radiative processes, soil moisture and a comprehensive hydrologic cycle. The solar radiation arriving at the top of the model atmosphere is regulated according to the seasonal cycle. The cloud cover is prescribed and is assumed to be a function of height and latitude only.

In the model integrations described here, the SST conditions in the tropical Pacific basin between 30°N and 30°S (i.e., the region depicted by light shading in Fig. 1) were constrained to follow the observed SST variations during the 15-year period from January 1962 to December 1976. In Fig. 2 is shown the time series of the departure from normal of SST averaged over the region extending from 4.5°S to 4.5°N, 176.25°E to 138.75°W (i.e., the strip indicated by heavy shading in Fig. 1). It is seen from this figure that the 15-year time span considered here encompasses four complete ENSO events, with warm SST anomalies along the central equatorial Pacific peaking toward the end of 1963, 1965, 1969 and 1972. In between these individual warm events are periods of cold anomalies, such as those occurring at the end of 1964, 1970 and 1973.

Within the shaded zone in Fig. 1, the temporal changes of SST were reconstructed by adding the climatological observations documented by the U.S. Naval Oceanographic Office to the data for SST anomalies in 1962–76. The data for SST anomalies were compiled at the Climate Analysis Center (CAC), and were made available to us through the kind arrangements of E. M. Rasmusson and T. H. Carpenter. Details on the data source and analysis methods used are described in Rasmusson and Carpenter (1982). The original data set from CAC, which consists of monthly mean values with a resolution of 2° in both the zonal and meridional directions, was reanalyzed on a coarser 4.5° × 7.5° latitude–longitude mesh so as to be compatible with the model Gaussian grid. The time series at each grid point was then smoothed using a 1:2:1 filter. Daily values were computed by linear interpolation between the monthly averaged observations, with the assumption that the data for the 15th day of each month is equal to the monthly mean value for that month. The GCM integrations were conducted through the entire 15-year period by updating the tropical Pacific SST conditions every model day. At oceanic grid points lying outside of the region depicted by light shading in Fig. 1, the SST values were prescribed to evolve through 15 identical annual cycles, as inferred from the observed climatology provided by the U.S. Naval Oceanographic Office. Hence, no interannual variability has been introduced in the SST of the world oceans other than the tropical Pacific.

Altogether two 15-year integrations were conducted in the manner described above. The only distinction between these two experiments is that they start from different initial atmospheric conditions. This pair of integrations hence represents two independent realizations of the model climate subjected to the same sequence of changing boundary forcing. The rationale for repeating the 15-year integration a second time is to double the size of the data sample, so that the statistical significance of various simulated features is enhanced. Comparison between data from the two individual runs would also provide information on how reproducible the model response is to a given set of SST conditions. The two sets of atmospheric initial conditions used in the present study were derived from

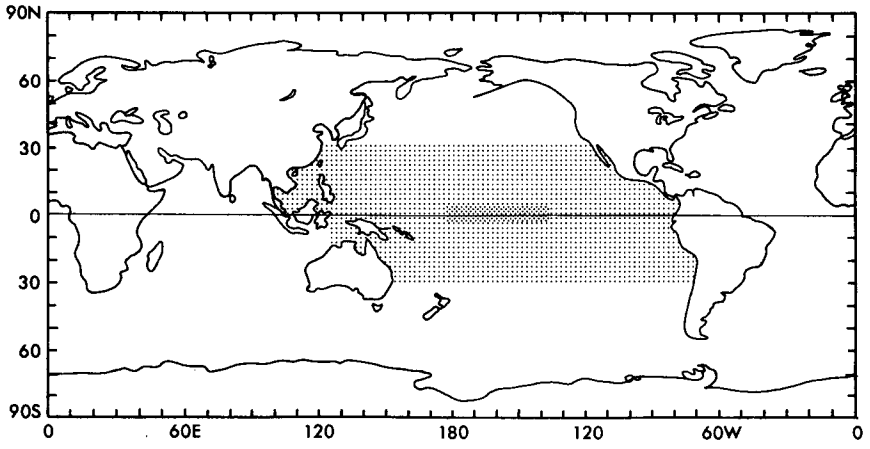

FIG. 1. Light shading indicates the region where observed sea surface temperature variations during 1962–76 are imposed at the lower boundary of the model. Dark shading indicates the region selected for computing the spatial averages of sea surface temperature presented in Fig. 2.

the 1 January data for two randomly selected years in the extended model experiment previously analyzed by Manabe and Hahn (1981) and Lau (1981). The latter experiment, which has a total duration of 17.75 model years, was conducted with essentially the same GCM as described here, except that no interannual variability in the SST conditions has been imposed anywhere in the world oceans.

3. Seasonal dependence of the 30-year model climatology

In view of the strong relationship between the evolution of an ENSO episode and the regular annual cycle, we shall first examine the model performance in simulating the seasonal dependence of various climatological circulation features. The presentation here is devoted to those meteorological parameters that are most directly associated with ENSO phenomena. All results shown in this section are based on 30-year averages of the pair of 15-year model integrations described in Section 2.

a. 950 mb wind

In Fig. 3 is shown the climatological distribution of the horizontal wind vectors at 950 mb during (a) January and (b) July. Regions of horizontal convergence are depicted by shading. The letters "H" and "L" indicate the locations of high and low centers in the corresponding sea level pressure fields. The latter patterns (not shown) are almost identical to those presented by Manabe and Hahn (1981, their Figs. 4.1 and 4.2) based on a different long-term run with the same GCM.

The most pre-eminent features in Fig. 3 are the seasonal reversal of the surface wind direction associated with the monsoonal circulations in south and east Asia, northern Australia, and western Africa situated between 5° and 20°N. The circulation over much of the tropical Pacific and Atlantic is dominated by the northeasterly and southeasterly trades. These two trade-wind systems meet each other near the equator, forming well-defined intertropical convergence zones (ITCZs). Notwithstanding the coarse resolution of the model grid (approximately 4.5° in latitude), it is still possible to discern seasonal migration of the ITCZs in the meridional direction, with much of the convergence zones in January (Fig. 3a) being located south of their corresponding July (Fig. 3b) positions. Such seasonal shifts are particularly marked over the Indonesia–Australian and South America–Atlantic sectors.

In January, the easterlies over the tropical Pacific south of the equator are interrupted near the date line by the South Pacific Convergence Zone (SPCZ) extending southeastward from North Australia–New Guinea toward the midlatitude South Pacific (see thick dashed line in Fig. 3a). An analogous feature extending southeastward from the Brazilian coast at about 25°S is also evident in the South Atlantic during January. In July (Fig. 3b), the SPCZ appears to be weaker, and easterlies prevail over virtually the entire equatorial Pacific Basin, except for the region of weak circulation east of the Philippines, where the easterly trades meet the southwesterly summer monsoon over South Asia.

The circulation and convergence characteristics of

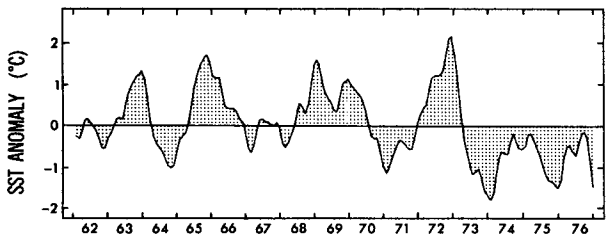

FIG. 2. Temporal variation of sea surface temperature anomaly averaged over the region from 4.5°S to 4.5°N and from 176.25°E to 138.75°W (indicated by dark shading in Fig. 1) during 1962–76.

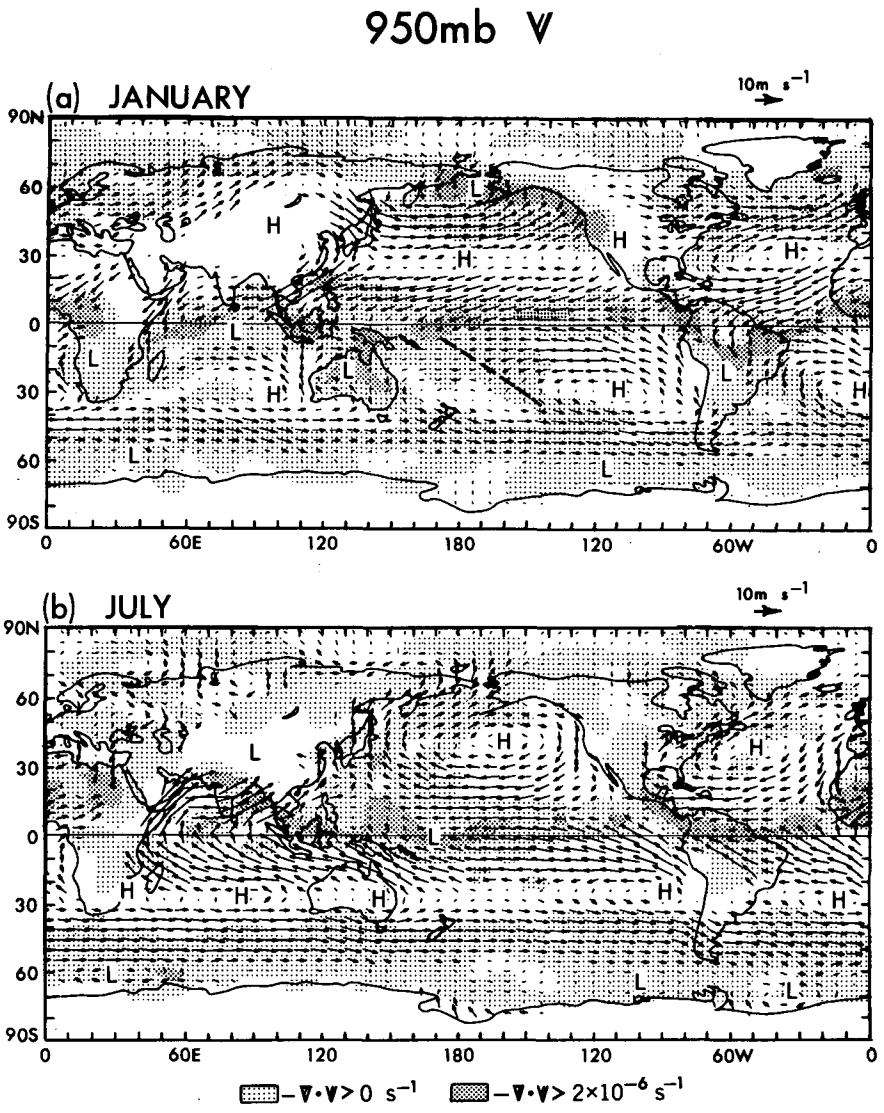

FIG. 3. Arrows depict the climatological vector wind field at 950 mb. Scale of arrows is given at the upper right corner of each panel. Light and dark shading indicates convergence exceeding 0 and 2×10^{-6} s^{-1}, respectively. Arrows are not shown over land surfaces lying above the 950 mb level. "H" and "L" indicate positions of the high and low centers in the climatological sea level pressure field. All data shown are based on averages over the calendar months of (a) January and (b) July for 30 simulated annual cycles. Dashed line in panel (a) indicates the location of the South Pacific Convergence Zone.

the surface flow noted above may be compared with the observed climatology documented by Oort (1983, Fiche F-23) for the entire globe, and by Wyrtki and Meyers (1976, Figs. 1 and 2) and Rasmusson and Carpenter (1982, Figs. 4 and 5) for the tropical Pacific. Whereas most of the principal features are discernible in both observed and simulated atmospheres, it is worth noting that the model ITCZ in the South America–Atlantic sector is located slightly south of the observed position, and that the observations portray a more marked seasonal change in the meridional position of the Pacific ITCZ.

b. 200 mb streamfunction

The rotational component of the time-mean flow at 200 mb is depicted by the global distribution of the streamfunction in Fig. 4, for the (a) December–February and (b) June–August seasons. In constructing these figures, the zonal mean for each latitude circle has been removed from all data points along that circle.

The patterns of the streamfunctions in both seasons may be compared with the observed geopotential height distributions presented by Wallace (1983, Figs. 2.2 and 2.7 for the Northern Hemisphere and Figs. 2.13 and

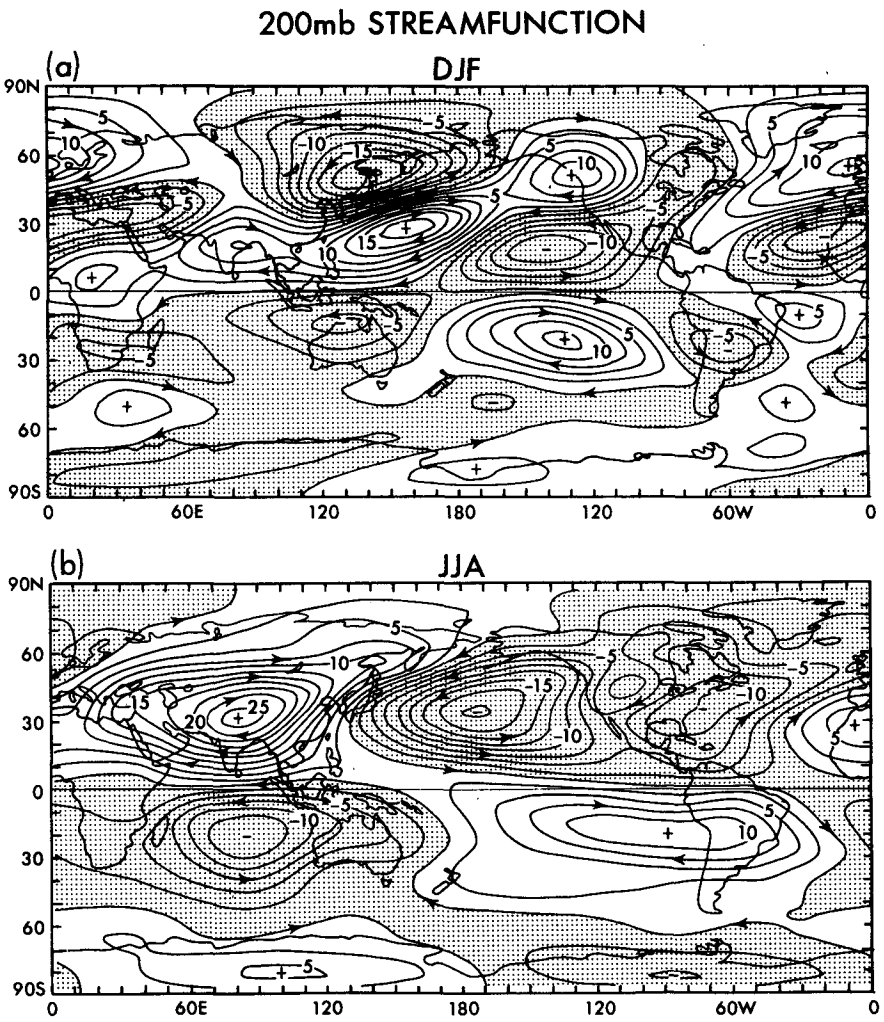

FIG. 4. Distributions of the departure from zonal symmetry of the climatological streamfunction at 200 mb, as obtained by averaging wind data over the seasons of (a) December–February and (b) June–August for 30 simulated annual cycles. Contour interval 2.5 × 10^6 m^2 s^{-1}. Shading indicates negative values. The rotational flow component circulates in a clockwise fashion around maxima, and in a counterclockwise fashion around minima.

2.17 for the Southern Hemisphere), noting that a contour interval of 60 m in geopotential height is approximately equivalent to a contour interval of 6 × 10^6 m^2 s^{-1} in the streamfunction field at 45° latitude. In the wintertime Northern Hemisphere (Fig. 4a), the amplitude of the simulated stationary trough over eastern Canada is weaker than its observed counterpart. In the summertime Northern Hemisphere (Fig. 4b), the simulated trough in the Atlantic sector is displaced too far west of its observed position, and there is little evidence in the simulation of the cold trough over eastern Canada and the North Atlantic ridge, as noted by White (1982) and Wallace (1983).

In the wintertime Southern Hemisphere (Fig. 4b), the observations indicate an abrupt change in the longitudinal phase of the perturbations at about 45°S, whereas the transition zone for the simulated atmosphere is located at 60°S. In both winter and summer seasons, the simulated stationary wave amplitude in the high latitudes of the Southern Hemisphere is substantially weaker than that observed.

In summary, the GCM is capable of simulating the streamfunction field in the wintertime Northern Hemisphere with a reasonable degree of fidelity; whereas some discrepancies between model and observations exist in the Southern Hemisphere and in the summertime Northern Hemisphere.

c. 200 mb velocity potential

In Fig. 5 are shown the simulated distributions of the velocity potential at 200 mb during the (a) December–February and (b) June–August seasons. The divergent flow component and the horizontal divergence are respectively given by the gradient and Laplacian of

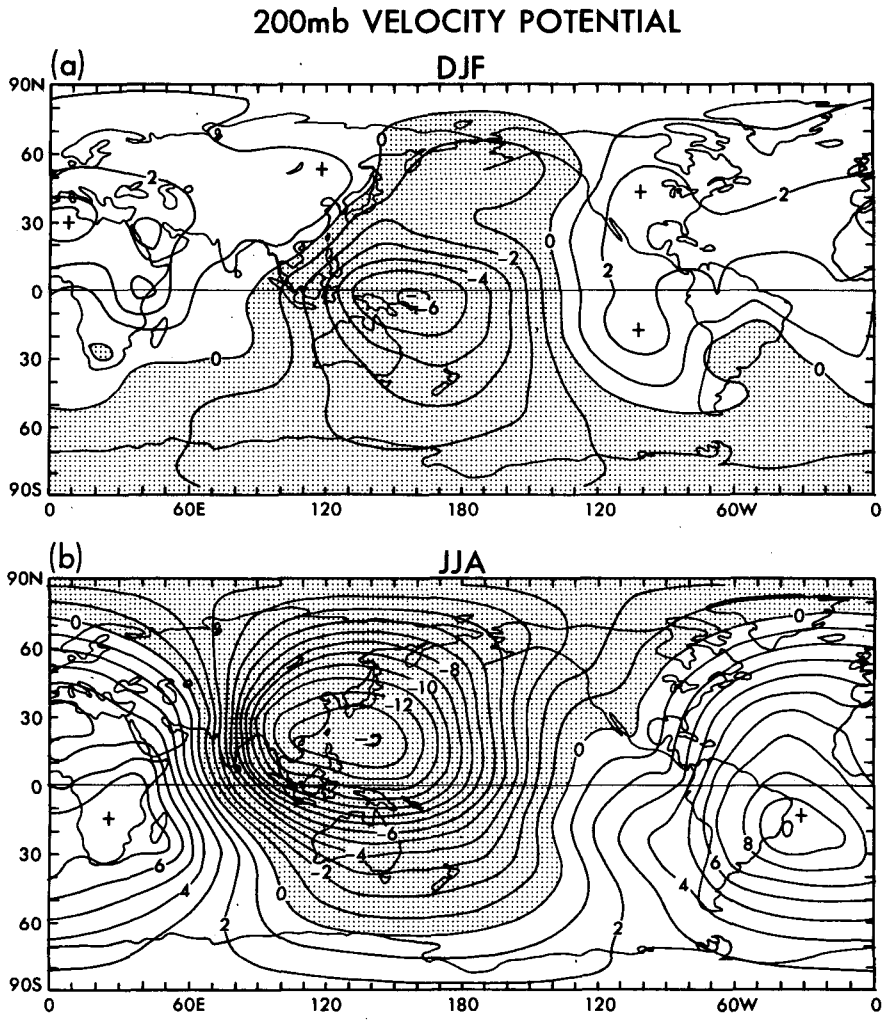

FIG. 5. As in Fig. 4 except for the velocity potential at 200 mb and with the zonal mean values retained. Contour interval 1×10^6 m^2 s^{-1}. Divergent flow component is directed perpendicular to the contours towards higher values.

the fields shown here. The velocity potential is therefore a convenient indicator of the pattern of large-scale divergent motions. The pattern for the DJF season (Fig. 5a) is dominated by a dipole-like structure over the tropical Pacific, with a center of minimum just east of New Guinea, and a maximum elongated in the meridional direction and situated at approximately 100°W. During the JJA season (Fig. 5b), the center of minimum over the western Pacific is located north and west of its DJF position, whereas much of the South Atlantic, South America and South Africa are under the influence of a broad maximum in the velocity potential field.

The model results shown here may be compared with the observed patterns for single seasons, as presented by Krishnamurti (1971, Fig. 1), Krishnamurti *et al.* (1973, Fig. 1), Lau (1984a,b) and Sardeshmukh and Hoskins (1985). The position of the minimum over the western Pacific, as simulated by the model, is displaced considerably east of that depicted by Krishnamurti's charts, but agrees well with the positions inferred from FGGE Level III-B analyses (Lau 1984a,b), and from operational analyses produced by ECMWF (Sardeshmukh and Hoskins, 1985). During the DJF seasons, the divergent flows associated with the ITCZs over the equatorial oceans, as well as the outflow corresponding to intense convective activity over Indonesia, central Africa and South America, are generally stronger and show up more clearly in the observed patterns than in the simulation. The observed velocity potential fields generally possess a more detailed structure in the meridional direction; whereas the longitudinal phase of the model patterns in Fig. 5 exhibit little variation with latitude.

d. Precipitation

The 30-year mean distribution of simulated precipitation is shown in Fig. 6 for (a) January and (b) July. The heaviest rainfall in January is seen to occur within the ITCZs over the equatorial oceans, the Indonesian

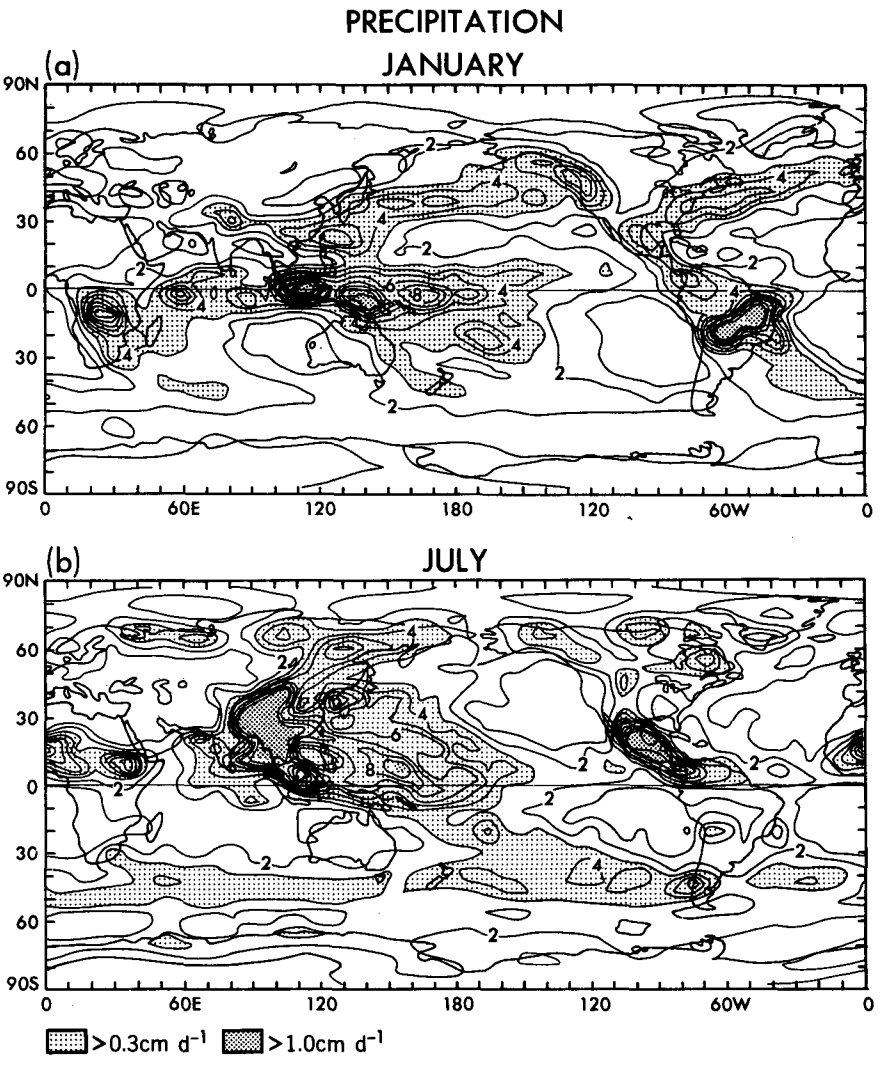

FIG. 6. Distributions of the climatological precipitation rate, as obtained by averaging over the calendar months of (a) January and (b) July for 30 simulated annual cycles. Contour interval 0.1 cm d^{-1}. Light and dark shading indicate precipitation rates exceeding 0.3 and 1 cm d^{-1}, respectively.

Archipelago, the Congo Basin and Brazil. Also evident in Fig. 6a is the enhanced precipitation accompanying the SPCZ (see dashed line in Fig. 3a). The pattern in the wintertime Northern Hemisphere extratropics is characterized by the elongated maxima spanning the Pacific and Atlantic at approximately 40°N. These midlatitude rainbelts coincide with the preferred tracks of migratory synoptic scale storms (e.g., see Lau, 1981, Fig. 2). In July (Fig. 6b), the rainfall maxima in the tropics are shifted northward relative to their January positions. There is also evidence of enhanced precipitation along the wintertime cyclone tracks at 50°S (e.g., see Trenberth, 1981, Fig. 17b). Both Figs. 6a and 6b indicate that dryness prevails over the eastern oceans in the summer hemisphere, when the local surface circulation is dominated by anticyclones (see Fig. 3).

The model patterns shown here may be compared with the global climatological rainfall charts compiled by F. Möller and reproduced in Manabe and Holloway (1975, Figs. 13 and 14). More recently, Dorman and Bourke (1979, Figs. 5 and 7; 1981, Figs. 5 and 7) have documented the precipitation patterns over much of the Pacific and Atlantic on the basis of ship observations. The distribution of rainfall in the tropics may also be indirectly inferred from data on outgoing longwave radiation as collected by satellites (e.g., see Heddinghaus and Krueger, 1981, Fig. 3). Whereas most of the observed large-scale features and their seasonal movements are reproduced by the model, it is seen that the simulated ITCZs are not as clearly identifiable as their observed counterparts. In particular, the GCM severely underestimates the precipitation along the ITCZ over the Atlantic and eastern Pacific. Another notable discrepancy is the much heavier precipitation

over the Tibetan Plateau in the model atmosphere, especially during the summer season.

e. Seasonal migration of the ITCZ over the Eastern Pacific

The seasonal dependence of the latitudinal position of the climatological ITCZ over the eastern Pacific is examined in greater detail in Fig. 7, which depicts the time–latitude distribution of the 30-year mean (a) 950 mb horizontal convergence and (b) precipitation. The patterns shown here are based on model data averaged over the longitudinal zone extending from 108.75°W to 131.25°W. This particular zone is chosen here by virtue of its proximity to the sites where typical warm SST anomalies associated with ENSO episodes first appear during the boreal spring (see Rasmusson and Carpenter, 1982, Fig. 19). Arguments presented by Philander (1983) also suggest that the subsequent evolution of these warm water episodes crucially depends on the meridional position of the local climatological ITCZ in the northern spring. In both figures annual mean values have been subtracted from the data for individual calendar months to obtain deviations.

Figure 7 indicates that low-level convergence and precipitation exhibit a well-defined annual cycle within the zone between 15°S and 5°N, with the maximum occurring in March–April and the minimum in September–October. The surface convergence and precipitation associated with the ITCZ in this region hence reach their southernmost extent during the northern spring. In regions located immediately north of 5°N, the phase of the annual cycle in 950 mb convergence is almost exactly opposite to that in the Southern Hemisphere tropics (Fig. 7a). The phase relationships shown here are in agreement with the spatial dependence of observed annual cycles, as documented by Horel (1982, Fig. 4) for surface wind convergence, and by Dorman and Bourke (1979, Fig. 10) for precipitation. However, the amplitude of the annual cycle in the simulated surface convergence (Fig. 7a) is only about 50% of the observed value.

Inspection of diagrams similar to Fig. 7 but with the annual means retained (not shown) indicates actual southward migration of maxima in precipitation and surface convergence during the northern spring, and actual northward retreat of these maxima 6 months later. The annual cycle depicted in Fig. 7 hence reflects the seasonal displacement of the Pacific ITCZ in the meridional direction, rather than the presence of geographically-fixed features with seasonally varying amplitudes. At 5°S, the amplitude of the seasonal cycle in convergence and precipitation (1×10^{-6} s^{-1} and

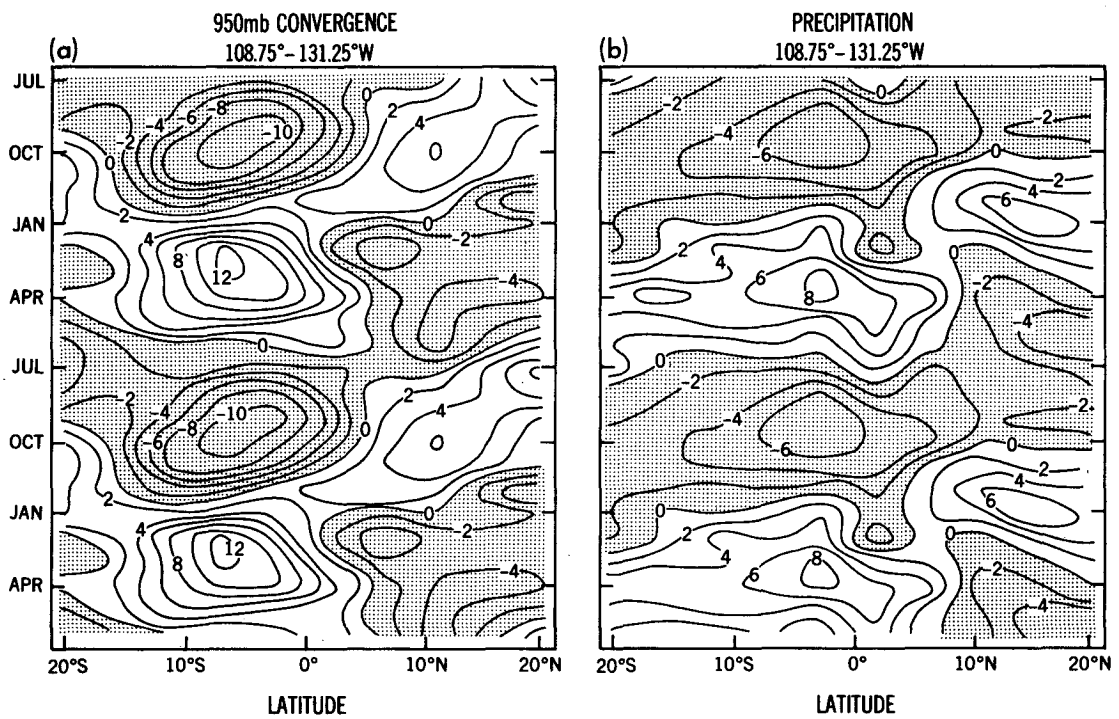

FIG. 7. Distributions of departures from annual mean of climatological (a) horizontal convergence at 950 mb, contour interval 2×10^{-7} s^{-1}, and (b) precipitation rate, contour interval 0.02 cm d^{-1}, based on spatial averages in the belt between 108.75°W and 131.25°W, and plotted as functions of calendar month and latitude. Shading indicates negative values. Positive values in (a) denote above-average convergence or below-average divergence.

0.07 cm d^{-1}, respectively), is quite comparable with the corresponding annual means (approximately 1 $\times 10^{-6}$ s^{-1} and 0.1 cm d^{-1}).

4. Time series of selected circulation indices of the model atmosphere

In Fig. 8 are shown the variations of selected model parameters during the entire length of the two 15-year simulations. Some of the indices displayed here are chosen to depict the circulation characteristics in certain key regions, where anomalous model behavior is particularly prominent. Other model indices shown are constructed in a manner similar to that prescribed in selected observational studies. The circulation indices presented in Fig. 8 include:

- SST averaged over the equatorial Pacific from 4.5°S to 4.5°N, and from 176.25°E to 138.75°W. The variation of SST anomalies has already been shown in Fig. 2, and is identical in the two 15-year runs examined here.
- Zonal wind at 200 mb and 950 mb, averaged over the equatorial Pacific from 4.5°S to 4.5°N, and from 168.75°E to 146.25°W.
- Precipitation averaged over the equatorial Pacific from 4.5°S to 4.5°N, and from 176.25°E to 138.75°W.
- The Southern Oscillation Index, as obtained by subtracting the 1000 mb height at Darwin from the corresponding value at Tahiti (see Chen, 1982a for an assessment of various sea level pressure indices used in the observational literature). In constructing the model index, the locations of Darwin and Tahiti are assumed to correspond to the 15° (longitude) × 9° (latitude) patches centered at (13.5°S, 131.25°E) and (18°S, 146.25°W), respectively.
- The 200 mb height index for the tropics, as obtained by a linear combination of 200 mb height values at five tropical locations, i.e., $0.20Z^*$ (Nairobi) + $0.23Z^*$ (Darwin) + $0.23Z^*$ (Nandi) + $0.25Z^*$ (Hilo) + $0.27Z^*$ (San Juan), where Z^* denotes the departure from normal of the height values for a given month, as normalized by the standard deviation of the local height fluctuations for that calendar month. The definition of this index follows that devised by Horel and Wallace (1981, Eq. 1), and serves as a convenient indicator of the thickness between 1000 and 200 mb along the tropical belt. In constructing the 200 mb height index using model data, the locations of Nairobi, Darwin, Nandi, Hilo and San Juan are assumed to be the 15° (longitude) × 9° (latitude) patches centered at 0°, 41.25°E; 13.5°S, 131.25°E; 18°S, 176.25°E; 18°N, 153.75°W; and 18°N, 63.75°W, respectively.
- The 700 mb height index for the PNA pattern, as obtained by the expression Z^* (54°N, 116.25°W) $-$ ½[Z^* (45°N, 161.25°W) + Z^* (31.5°N, 86.25°W)]. This definition follows that used in the study by Horel and Wallace (1981) for portraying the intensity and polarity of the characteristic circulation pattern over the North Pacific–North American sector. Averages of the model data over 15° (longitude) × 9° (latitude) patches centered at the locations indicated in the above formula are used to compute the PNA index.

All indices displayed in Fig. 8 are constructed on the basis of anomalies, as obtained by subtracting the long-term mean for a given month from the model data for the same calendar month in individual years. The smooth curves superimposed on the raw time series are computed using the 15-point Gaussian filter described in Pan and Oort (1983, Fig. 5). Some time series for the first integration, with the monthly anomalies being normalized by the standard deviations, have been compared with the corresponding observations during the 1962–76 period by Lau and Oort (1985).

The time series in Fig. 8 illustrate the strong influence of the Pacific SST conditions on the circulation in the model tropics. For both 15-year runs, the warm water prescribed in the central equatorial Pacific towards the end of 1963, 1965, 1968, 1969 and 1972 is accompanied in the model atmosphere by below-normal 200 mb westerlies, above-normal 950 mb westerlies, and above-normal precipitation near the region of forcing, negative Southern Oscillation Index in sea level pressure, and above-normal 200 mb height throughout the tropics. Model response of the opposite sense is also evident in the cold water episodes during the northern winters of 1964/65, 1966/67, 1970/71 and 1973/74. Various model anomalies are seen to be of comparable amplitude in different events, especially in those episodes centered at the 1965, 1969 and 1972 El Niños. The apparent lack of correspondence between various tropical indices on monthly time scales (see the thin curves in Fig. 8), and the much higher coherence among these same indices for periods longer than a year (as portrayed by the thick smooth curves), are consistent with the cross-spectral calculations presented by Trenberth (1976) and Rasmusson and Carpenter (1982) using station observations. The two 15-year integrations exhibit notable differences in the detailed month-to-month variations. However, the low frequency response is highly reproducible in the separate model runs.

The correspondence between the SST forcing and the PNA index is seen to be much less discernible than that pertaining to the tropical indices discussed in the preceding paragraph. Whatever signal might exist in the PNA time series are obscured by the high degree of month-to-month variability inherent in the extratropical circulation. Interpretation of the linkage between the PNA pattern and anomalous oceanic conditions is further complicated by the strong seasonal dependence of the midlatitude response to tropical forcing, as will be evident from the composite charts in Section 5, and from the correlation statistics to be discussed presently.

The above discussions pertaining to the time series in Fig. 8 may be quantified by considering the simul-

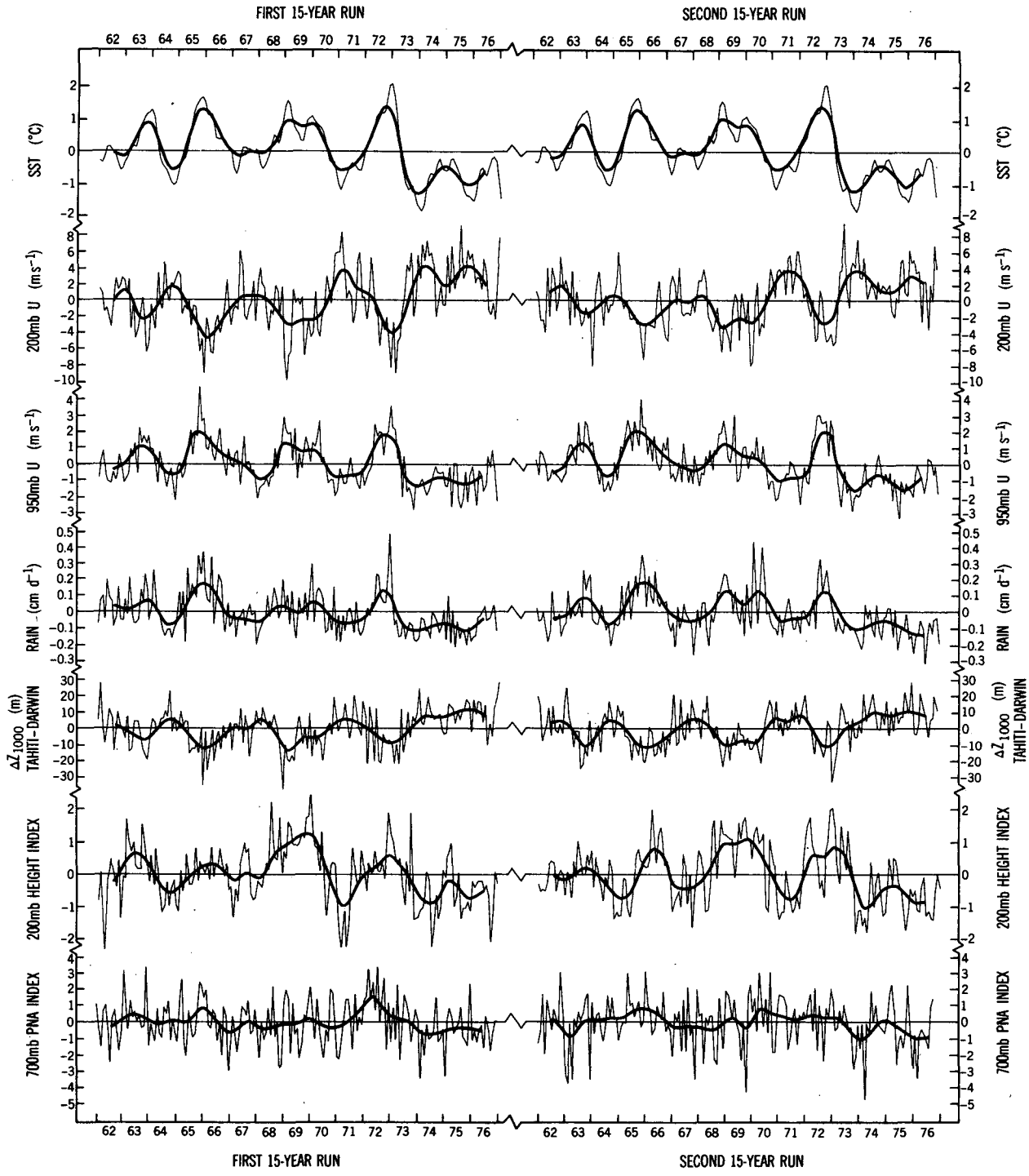

FIG. 8. Temporal variations of monthly indices of sea surface temperature, zonal wind at 200 and 950 mb, precipitation, east–west sea level pressure gradient across the South Pacific, 200 mb height and the Pacific–North American pattern, for the first (left half of figure) and second (right half) 15-year model runs. See text for definitions of indices. The smooth curves superimposed on these time series are obtained using a 15-point Gaussian filter.

taneous temporal correlation coefficients between the SST fluctuations and various circulation indices, as listed in Table 1. The statistics presented here are all obtained using seasonally averaged values. In addition to computing the correlations using all four seasons of the year, the corresponding values based on model data for only the northern summer and the northern winter in each 15-year integration are also shown, so as to

TABLE 1. Correlation coefficients (%) between SST variations in the equatorial Pacific and different circulation indices displayed in Fig. 8 (see definitions in text), as computed using seasonally averaged data for all 4 seasons of the year (first row), and for the northern summer (second row) and northern winter (third row) only. Statistics listed in the left (right) column under each circulation index are obtained using data for the first (second) 15-year model run.

	200 *U*		950 *U*		Precip		SOI		200 *Z*		PNA	
Year	−84	−81	89	90	85	84	−79	−75	66	67	42	32
JJA	−82	−74	86	95	84	67	−66	−81	57	26	9	14
DJF	−93	−93	87	91	91	90	−84	−72	77	85	53	45

delineate the seasonal dependence of such statistics. As a guide to assessing the statistical significance of the correlations tabulated here, application of Student's t-test to a sample size of 15 indicates that the threshold absolute values for the coefficients at the 95 and 99% confidence levels are 0.44 and 0.59, respectively.

Inspection of Table 1 confirms the strong relationship noted earlier between the indices for SST, zonal wind in the lower and upper troposphere, precipitation, sea level pressure and 200 mb height. The generally high level of correlation between SST variations and different tropical indices do not seem to exhibit any systematic seasonal dependence, with the exception in the case of the 200 mb height index, which shows a minimum correlation in the northern summer. When compared with the tropical circulation indices, the midlatitude PNA pattern exhibits a much weaker association with the SST variations. The correlation between the PNA and SST indices is considerably higher in winter than in summer.

The circulation statistics for the SST, precipitation, Southern Oscillation, 200 mb height and PNA indices in the northern winter compare favorably with the corresponding observed values published by Horel and Wallace (1981, Table 1). In particular, the latter study also yields a relatively weak correlation (0.46) between the observed wintertime SST and PNA indices. The lack of seasonal dependence in the correlation between the SST, precipitation and Southern Oscillation indices in the model atmosphere is substantiated by the data compilations of Wright (1977, Table 4 and Fig. 30).

5. Composite charts of model anomalies in a typical ENSO episode

The overall regularity and quasi-cyclic behavior of the model response to various El Niños in the 1962–76 period, as is evident from the time series displayed in Fig. 8, suggest that the construction of composite charts is a useful approach for describing the evolution of the simulated circulation in different phases of a typical ENSO episode. The epochs chosen for constructing these composite charts are those encompassing the El Niños in 1965, 1969 and 1972 (see Fig. 2). Since two independent GCM integrations have been conducted using the changing SST conditions for the same 15-year period, the composites shown here are averages over altogether six events. Data for the 1963 event are not used in view of its relatively weaker intensity and its proximity to the 1965 event. The occurrence of the 1976 event near the end of the 15-year period precludes its inclusion in this composite analysis. Following the convention adopted by Rasmusson and Carpenter (1982, hereafter referred to as RC) the label 0 is used to denote an El Niño year, the labels −1 and +1 are used to denote the years preceding and following an El Niño year, respectively, and so forth.

Composites of the anomalies in various parameters have been computed for each of the months during the 33-month period from June of year −1 to February of year +2. The model anomaly during a given month is defined as the departure from the 30-year climatology for that particular calendar month. Special emphasis is placed on the model behavior during the two-year period extending from the northern spring of year 0, which corresponds to the initiation of the warm SST anomaly off the Peruvian coast, to the beginning of year +2, when the cold SST anomaly spreads across much of the equatorial Pacific.

Statistical significance tests have been performed on the anomalous features appearing in some of the composite charts. These significance levels are determined by Student's t-statistic (e.g., see Chervin and Schneider, 1976), which is essentially the ratio of the anomaly strength to the square root of the "combined" variance of the data sample in question. The combined variance is in turn related to the standard deviation of the entire 30-year data sample as well as the variability among the six cases used in constructing the composite anomaly. In applying the *t*-test to the patterns in panels (b), (d) and (f) in Figs. 9, 10, 11, 12 and 14, the number of events incorporated in each seasonal composite (i.e., N_1 in Chervin and Schneider's notation) has been set equal to 6, the total number of seasons incorporated in the climatology (N_2 in Chervin and Schneider's notation) has been set equal to 30, and the number of degrees of freedom has been set equal to $30 - 2 = 28$. For the special case of the SST composites [panel (a) in Figs. 9, 10, 11, 12, 14 and 15], since the conditions prescribed at the lower boundary are identical in the two 15-year runs, the values of N_1 and N_2 have been set equal to 3 and 15, respectively, and the corresponding number of degrees of freedom is $15 - 2 = 13$. Since all streamfunctions differing from one another by an

arbitrary, spatially invariant constant satisfy the same Poisson's Equation, the statistical significance of 200 mb height anomalies is used instead to assess the confidence level of features appearing in the 200 mb streamfunction composite.

a. March (0)–April (0)–May (0)

In Fig. 9 are shown the distributions of the anomalies of (a) SST, (b) precipitation, (c) 950 mb horizontal wind vector (arrows) and divergence (shading), (d) 1000 mb

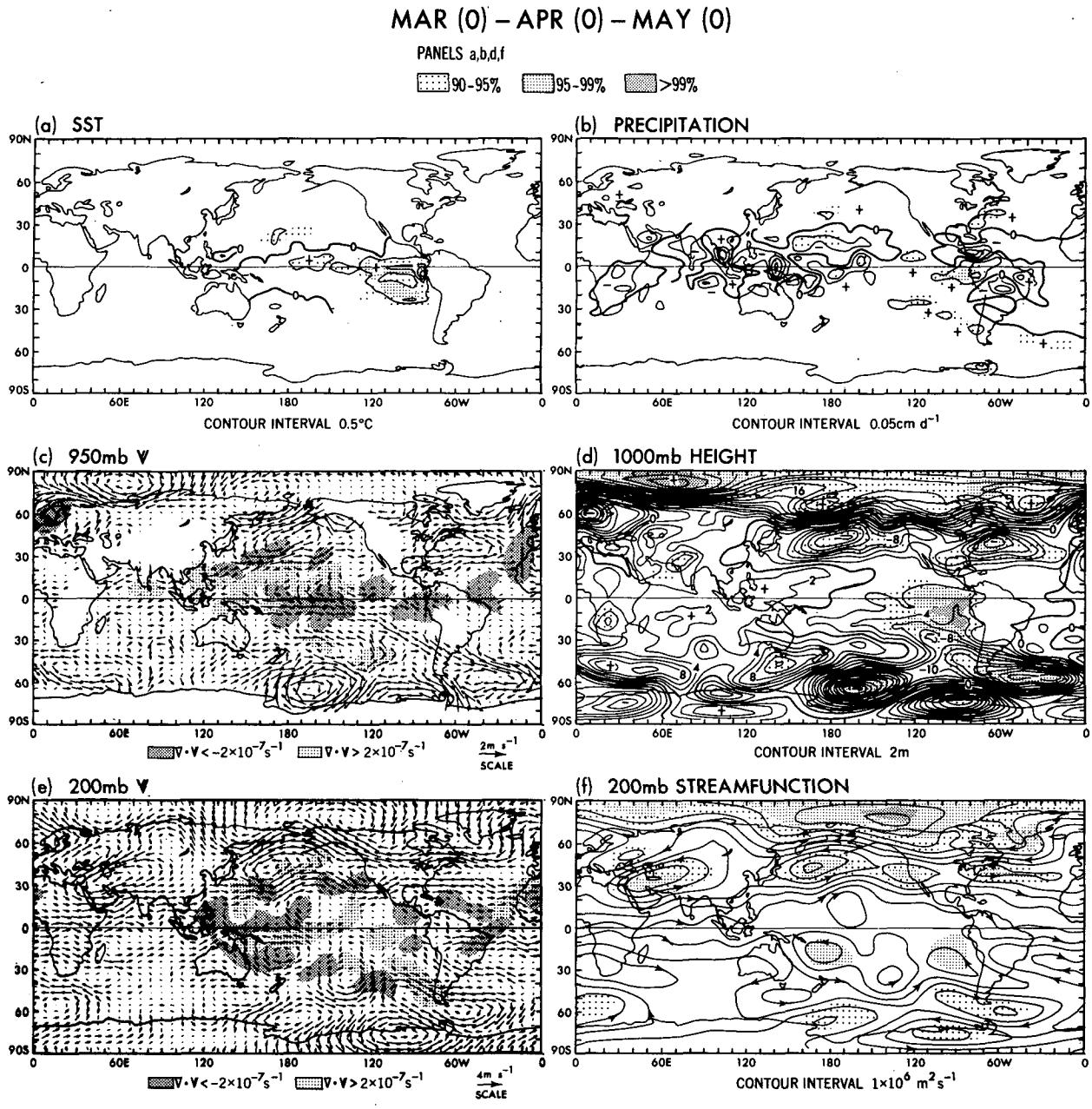

FIG. 9. Composite charts of departures from 30-year climatology of (a) sea surface temperature, contour interval 0.5°C, (b) precipitation rate, contour interval 0.05 cm d^{-1}, (c) horizontal wind vector at 950 mb, drawn according to scale at lower right corner, (d) 1000 mb height, contour interval 2 m, (e) horizontal wind vector at 200 mb, drawn according to scale at lower right corner, and (f) streamfunction at 200 mb, contour interval 1×10^6 m^2 s^{-1}, as constructed using simulated data for the period of March (0)–May (0) (see text for explanation of symbols) in 6 individual ENSO episodes. Light, medium and dark shading in panels (a), (b), (d) and (f) indicate anomalies exceeding the 90, 95 and 99% significance levels, respectively, according to Student's t-test. The significance of the 200 mb streamfunction field [panel (f)] is tested on the basis of 200 mb height anomolies (see text for details). Light and dark shading in panels (c) and (e) indicate divergence and convergence, respectively, with magnitudes exceeding 2×10^{-7} s^{-1}. For the sake of clarity, the zero-contours in panel (b) are omitted in some regions, and the positive and negative precipitation anomalies are identified by pluses and minuses, respectively.

height, (e) 200 mb horizontal wind vector (arrows) and divergence (shading), and (f) 200 mb streamfunction, as obtained by averaging model data for the 3-month periods centered on April of all 6 El Niño years (year 0). Precipitation, SST, 1000 mb height, and 200 mb height anomalies which exceed the 90%, 95% and 99% significance levels according to Student's t-test are indicated by various degrees of shading in panels (a), (b), (d) and (f), respectively. The same format will be used in Figs. 10, 11, 12 and 14 for displaying composite charts based on other time periods.

The positive SST anomalies just off the Peruvian coast reach their maximum strength during this season (Fig. 9a), and the climatological ITCZ over the eastern Pacific migrates to its southernmost position (Fig. 7). A tongue of low sea level pressure anomaly is simulated over the tropical South Pacific (Fig. 9d). The circulation accompanying this negative pressure anomaly is characterized by stronger than normal westerly surface flow along much of the Pacific Basin immediately south of the equator (Fig. 9c). The anomalous 950 mb circulation immediately north of equatorial Pacific exhibit a distinct northerly component, so that above-normal low-level convergence prevails along the equator and in regions farther south, whereas below-normal convergence prevails in regions farther north (Fig. 9c). These circulation features suggest a southward shift of the Pacific ITCZ in this period, a result also pointed out in the observational studies of Ramage (1975) and RC (their Fig. 19). This finding is further substantiated by the composite chart for precipitation (Fig. 9b), which exhibits a positive spatial correlation with the surface convergence field over the Pacific Basin.

The features in Fig. 9d lying in the Northern Hemisphere extratropics may be qualitatively compared with the corresponding composite charts presented by Chen (1982b, Fig. 13) using observed 700 mb height data for the period from 1951 to 1979. Both the observed and simulated patterns are characterized by below-normal heights over the midlatitude Pacific, the eastern Atlantic south of 40°N and Europe, and above-normal heights over Greenland and much of Canada.

The anomalous circulation at 200 mb in the model atmosphere (Figs. 9e and 9f) may be compared with the corresponding composite charts compiled by Arkin (1982, Fig. 9) using tropical NMC wind analyses for the 1969, 1972 and 1976 events. The anticyclonic circulation centered at approximately 20°S, 180°W is discernible in both the model and observed patterns. However, the cyclonic cell in the North Pacific is displaced too far west of the observed position, and considerable discrepancies exist over Eurasia.

b. June (0)–July (0)–August (0)

The composite charts for the northern summer of the El Niño years are shown in Fig. 10. This period is marked by a rapid expansion of the Pacific SST anomaly along the equator (Fig. 10a). The simulated precipitation near the equatorial South American coast, which has been above normal in the previous season (see Fig. 9b), is now seen to be near normal (Fig. 10b). Comparison between Figs. 9b and 10b also indicates that the precipitation over the equatorial Pacific near the date line has increased, and that continued dryness prevails in Indonesia, the western portion of the tropical Pacific, the Indian Subcontinent, and the highlands in western China. The subtropical features in Fig. 10b bear some resemblance to those in the composite presented by Lau and Chan (1983, Fig. 3a) on the basis of observed outgoing longwave radiation, and in the teleconnection chart presented by Wright (1977, Fig. 18) using rainfall records at selected stations. The negative precipitation anomaly over India is only significant at the 70–80% level in this simulation. It is, however, worth noting that Rasmusson and Carpenter (1983) and Shukla and Paolino (1983) have presented convincing empirical evidence on the suppressed summertime rainfall over that region during El Niño years.

The negative sea level pressure anomaly over the eastern portion of the subtropical South Pacific (Fig. 10d) has somewhat weakened since the previous season; whereas the sea level pressure in the Indonesia–North Australian sector has risen considerably. The anomalous east–west surface pressure gradient over the western portion of the tropical North Pacific is seen to be accompanied by local intensification of anomalous 950 mb westerlies (Fig. 10c). The overall pattern in Fig. 10d is in good agreement with the observed teleconnection charts based on various indices of the Southern Oscillation for this season, as presented by Wright (1977, Fig. 10).

The most prominent features in the 200 mb composite charts (Figs. 10e and 10f) are the pair of anticyclones on both sides of the equator, with easterly wind anomalies between 140°W and 160°E in the deep tropics, and westerly anomalies in the subtropical North and South Pacific. Above normal equatorial westerlies prevail east of the warm SST anomaly, and extend eastward across South America, the Atlantic and central Africa to the Indian Ocean. The presence of these features is substantiated by the observational composite presented by Arkin (1982, Fig. 10).

c. September (0)–October (0)–November (0)

This period is characterized by amplification of the warm SST anomaly in the eastern and central equatorial Pacific, and by diminution of the anomaly near the South American coast (Fig. 11a). Below normal rainfall prevails over Central America and the northern portion of South America (Fig. 11b). The dry zone extending southeastward from the Solomon Islands (located at approximately 10°S, 160°E), which appeared in the composites for the previous two seasons, is still evident in this period. To the northeast of this

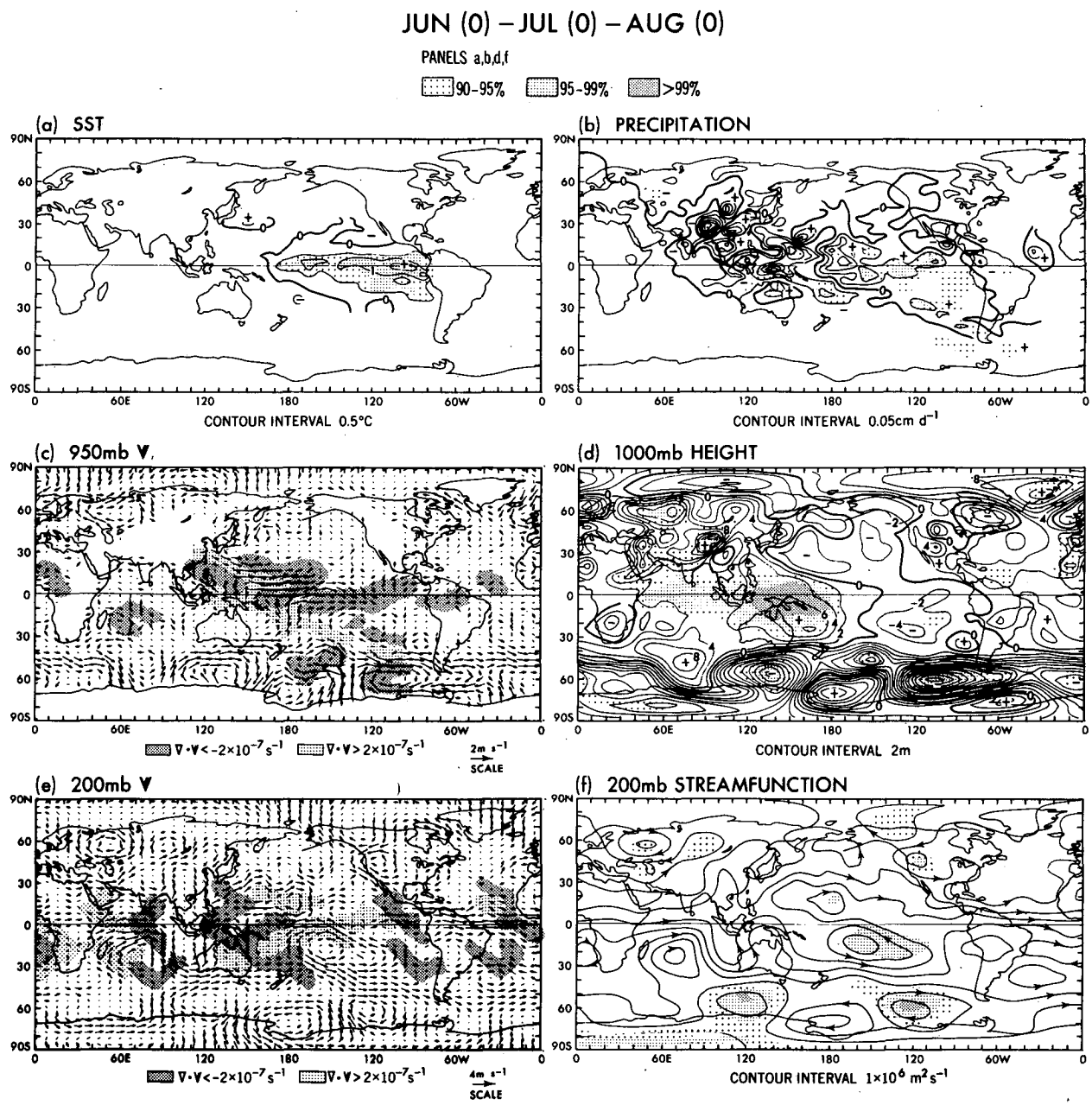

FIG. 10. As in Fig. 9 except for the period of June (0)–August (0).

dry zone is a belt of enhanced precipitation with a similar orientation. These features are consistent with the northeastward displacement of the observed SPCZ during this period (RC).

The near-surface circulation over the equatorial Pacific is characterized by a strong westerly wind anomaly west of 120°W, and by an easterly anomaly farther east (Fig. 11c). Low level convergence prevails over much of the warm SST anomaly. The afore-mentioned dry zone located southeast of the Solomon Islands is characterized by low-level divergence. Immediately east of this dry zone the anomalous surface flow is distinctly cyclonic.

Over the Pacific Basin between 30°S and 30°N, the anomalous sea level pressure field (Fig. 11d) is characterized by above normal values west of the date line, and below normal values farther east. In agreement with the observed 700 mb height composite charts for this period (Chen, 1982b, Fig. 11), the pressure over much of the North Pacific and eastern Europe is below normal, while the Alaska–west Canadian sector is characterized by positive height anomalies.

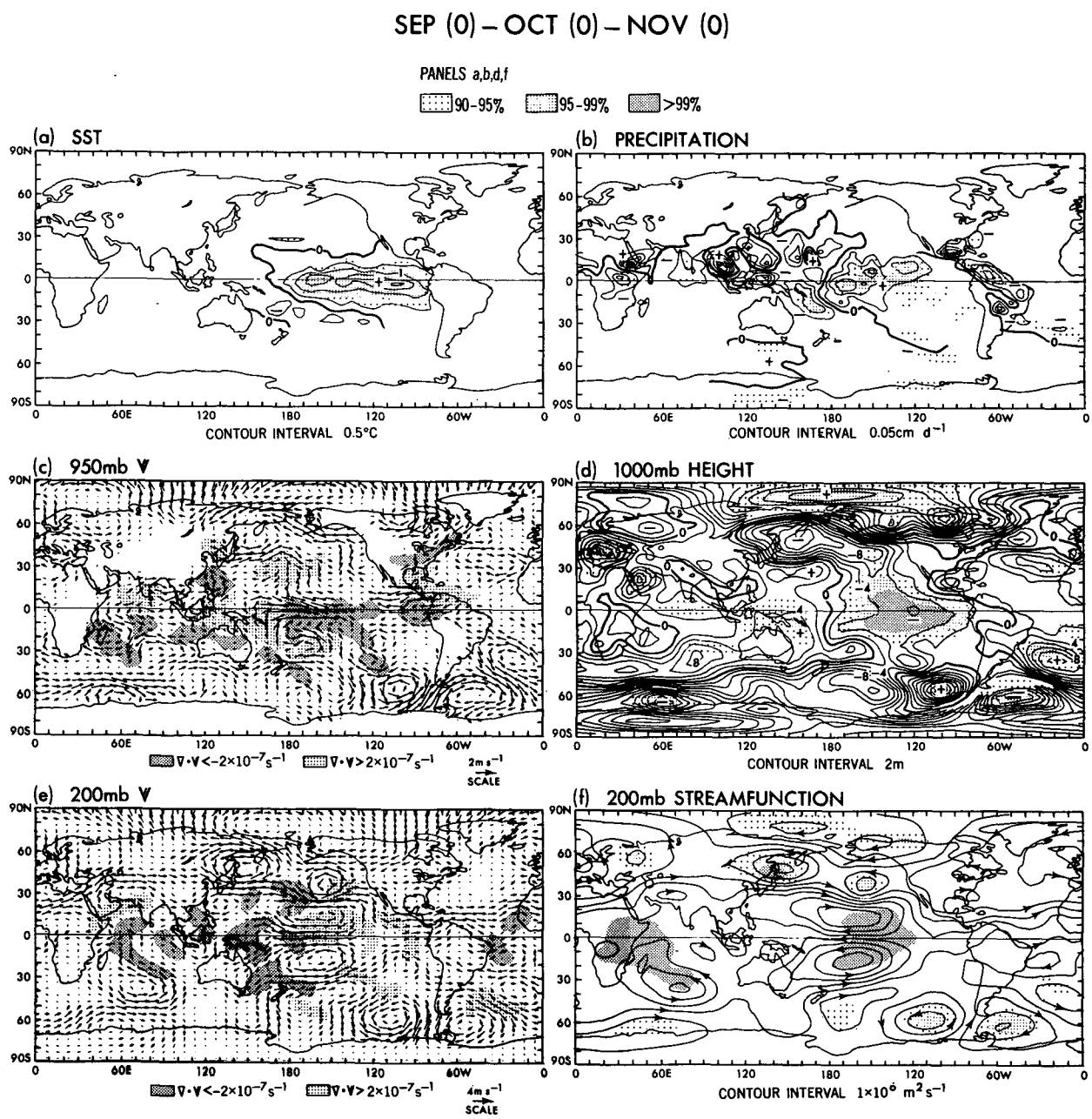

FIG. 11. As in Fig. 9 except for the period of September (0)–November (0).

In the 200 mb composite charts (Figs. 11e and 11f), the pair of Pacific anticyclones straddling the equator is now firmly established. A well-defined Southern Hemisphere wave train composed of alternating cyclonic and anticyclonic centers is seen to emanate from the central equatorial Pacific. The individual centers, most of which exceed the 95% significance level, lie along a curved path advancing towards the South Atlantic through the Drake Passage region. These centers are also accompanied by statistically significant anomalies of the same polarities at 1000 mb (Fig. 11d), thus indicating that perturbations along the wave path are characterized by an equivalent barotropic structure.

d. December (0)–January (+1)–February (+1)

In Fig. 12 are shown the composite charts for the northern winter following El Niño, which is referred to as the mature phase by RC. The enhanced precipitation along the equatorial Pacific now advances westward to almost 150°E (Fig. 12b). The zonal axis of this elongated anomaly tends to lie slightly south of the

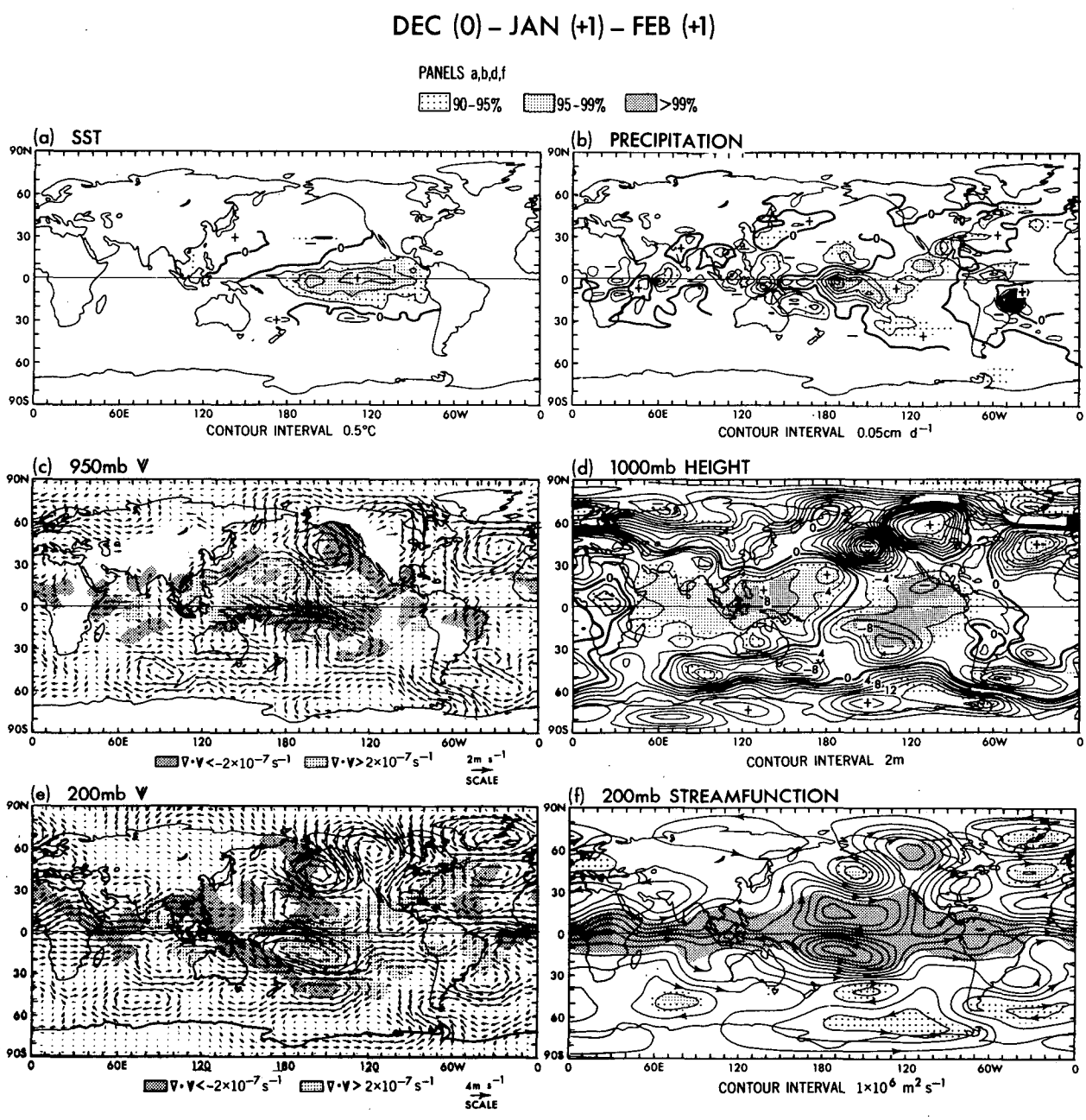

FIG. 12. As in Fig. 9 except for the period of December (0)–February (+1).

equator. Located east of the main anomaly are two narrow bands of above normal rainfall extending towards the subtropics. One of these bands is oriented southeastward and is associated with the northeastward shift of the SPCZ noted in the previous subsection. The other band lies in the Northern Hemisphere, and is directed toward Central America and the Gulf of Mexico. The southern two-thirds of Brazil is under the influence of a strong positive precipitation anomaly. Most of the simulated features identified above are consistent with analyses of the observed outgoing longwave radiation, as performed by Heddinghaus and Krueger (1981, Fig. 9) and by Lau and Chan (1983, Fig. 2a). The pattern of Fig. 12b in the tropics also agrees with the teleconnection chart presented by Wright (1977, Fig. 16) for precipitation during the northern winter. The enhancement of simulated rainfall over northern Mexico and the U.S. Gulf coast is substantiated by the observational records analyzed by Rasmusson and Wallace (1983, Fig. 1).

The anomalous 950 mb westerlies in the western and central equatorial Pacific attain their maximum

strength in this period (Fig. 12c). The wind vectors in this region are distinctly oriented toward the Southern Hemisphere, and are accompanied by strong anomalous convergence south of the equator along a zone extending from New Guinea to 120°W. The southerly surface flow over eastern China and the predominately offshore circulation along the east coast of Australia are consistent with the observed weakening of the monsoons in those regions (see RC, section 5e).

The 1000 mb height anomalies at both ends of the seesaw across the subtropical Pacific have amplitudes of more than 8 m (equivalent to 1 mb in sea level pressure) and generally exceed the 99% significance level (Fig. 12d). A belt of significant positive values is simulated along 20°N between the Philippines and 165°W. The presence of this feature in the observed atmosphere is supported by the teleconnection chart compiled by Wright (1977, Fig. 8) for the northern winter. The pattern in Fig. 12d may also be compared with its observed counterparts as presented by van Loon and Madden (1981, Figs. 11 and 14), Trenberth and Paolino (1981, Fig. 8a), and Pan and Oort (1983, Fig. 11d). In the Northern Hemisphere, both observed and simulated results indicate that the mature phase of ENSO (referred as the "low/wet" seasons in van Loon and Madden's study) is characterized by negative pressure anomalies over the eastern portion of the North Pacific, the northern portion of Asia and eastern North America, and by a positive anomaly over North America centered at about 50°N, 100°W. The observed pattern in the North Atlantic is dominated by a dipole-like structure, with a positive anomaly centered at the Norwegian Sea, and a negative anomaly in the middle latitudes. These polarities are seen to be reversed in the dipole appearing in the simulation (Fig. 12d). It is, however, worth noting that van Loon and Madden (1981, Figs. 3 and 4) have examined the meteorological anomalies associated with ENSO episodes occurring in four nonoverlapping subperiods of the last century. Their results indicate that the polarities of the sea level pressure anomalies over much of the extratropical North Atlantic were not uniformly the same during different subperiods, thus implying considerable variability of the observed atmospheric response in that region.

In the Southern Hemisphere, the model and observations yield negative pressure anomalies over the subtropical South Pacific as well as the oceanic regions lying between Australia and Antarctica. In the polar cap south of 50°S, a positive pressure anomaly is discernible in the observations presented by van Loon and Madden (1981, Fig. 11) as well as in the model simulation. The intensity of the anomalies in the model atmosphere is somewhat weaker than the observed values reported by van Loon and Madden.

At 200 mb, the Pacific anticyclones on both sides of the equator (Figs. 12e and 12f) attain their maximum intensity in this season. Upper level divergence is seen to prevail over the central equatorial Pacific. A meandering westerly current dominates the circulation in the equatorial zone lying outside of the central Pacific. The simulated pattern in the tropics agrees well with the composite compiled by Arkin (1982, Fig. 7) based on observed data.

The circulation in the Northern Hemisphere extratropics is organized about a wave train extending northeastward from the equatorial Pacific to North America, and then southeastward to the Atlantic sector. The locations of the cyclonic centers in the North Pacific and southeastern United States, and the anticyclonic center over western Canada, agree with the locations of the centers of action associated with the observed Pacific–North American (PNA) pattern studied by Wallace and Gutzler (1981), Horel and Wallace (1981), and Chen (1982b). Inspection of the composite charts for various seasons in year 0 (Figs. 9–12) indicates that the PNA response is essentially a wintertime phenomenon in the model atmosphere. The apparent seasonal dependence of this extratropical signal is consistent with the correlation statistics displayed in the last two columns of Table 1. The equivalent barotropic character of the PNA signal can be seen from the strong resemblance of the anomaly patterns at 1000 mb (Fig. 12d) and 200 mb (Fig. 12f).

The differences between the observed and simulated response over the North Atlantic in the middle and upper troposphere (Fig. 12f) are similar to the differences at the 1000 mb level noted earlier. Specifically, the polarities of the simulated height anomalies over the Greenland–Iceland sector and the midlatitude Atlantic are opposite to those in the observed patterns. However, Chen (1982b, Fig. 8) has shown that the observed composite of height anomalies over the North Atlantic do not pass the 95% significance test, and the evidence presented by Rogers (1984, Fig. 12) suggests that the north–south seesaw pattern over the North Atlantic (often referred to as the North Atlantic Oscillation) is not well correlated with the Southern Oscillation. The 200 mb pattern in the Southern Hemisphere extratropics is also suggestive of a wave train in the South Pacific–South Atlantic sector. The individual centers associated with the latter phenomenon are not as well defined as those simulated in the previous season (Fig. 11f).

The shape and relative size of the extratropical wave perturbations examined here is more faithfully described in the polar stereographic charts in Fig. 13, which show the composites of the 500 mb height anomaly during the mature phase in the (a) Northern and (b) Southern Hemisphere. The statistical significance of various features in these patterns is again depicted by shading. The pattern of Fig. 13b in the Pacific and Indian Ocean sectors is in good agreement with the teleconnection chart presented by Mo and White (1985, Fig. 14b) using Australian analyses of the 500 mb height, and with the composite chart presented by

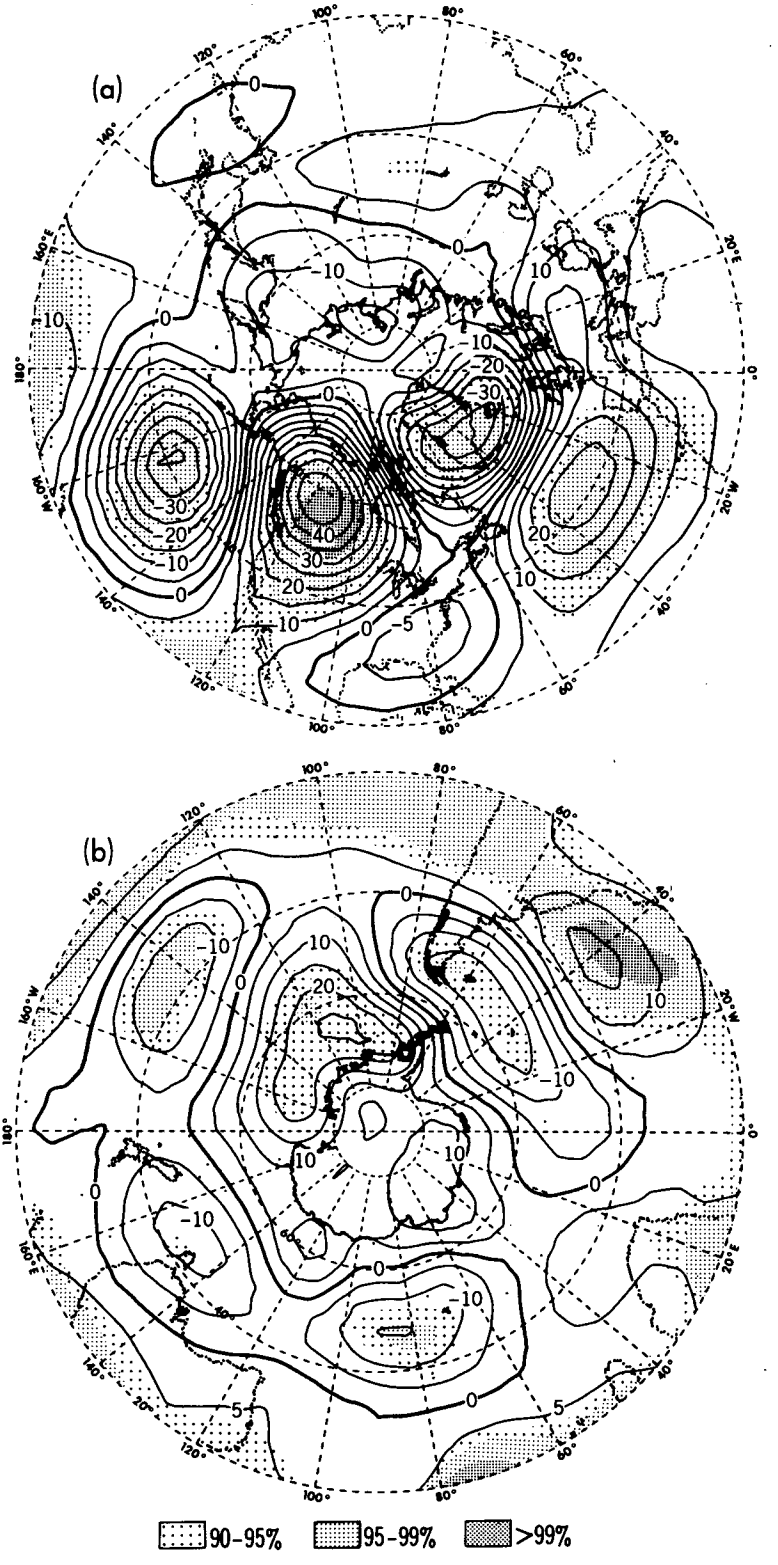

FIG. 13. Composite charts of the departure from 30-year climatology of 500 mb height in the (a) Northern Hemisphere and (b) Southern Hemisphere, as constructed using simulated data for the period of December (0)–February (+1) in 6 individual ENSO episodes. Contour interval 5 m. Light, medium and dark shading indicates anomalies exceeding the 90, 95 and 99% significance levels, respectively, according to Student's t-test.

van Loon and Rogers (1981, Fig. 7) using analyses of the zonal geostrophic wind at 500 mb.

The performance of other GCMs in simulating various ENSO phenomena in the mature phase has been documented by Blackmon *et al.* (1983), Shukla and Wallace (1983), Michaud and Sadourny (1984), Palmer and Mansfield (1984) and Boer (1985). The findings reported in these studies generally indicate that the current generation of models is capable of reproducing such essential features as precipitation changes and the sea level pressure seasaw over the tropical Pacific, as well as the PNA pattern in the midlatitudes.

e. December (+1)–January (+2)–February (+2)

The boreal spring of year (+1) sees a considerable weakening of the positive SST anomaly over the central equatorial Pacific, as well as the appearance of a cold anomaly just off the Peruvian coast (see RC, Fig. 23). The latter feature subsequently spreads across the Pacific. The circulation changes occurring in year (+1) are illustrated in Fig. 14, which contains a set of composite charts for the December (+1)–January (+2)–February (+2) season.

It is seen from Fig. 14a that much of the equatorial Pacific is now under the influence of an elongated negative SST anomaly. The precipitation pattern (Fig. 14b) indicates suppressed rainfall over the equatorial Pacific east of 160°E, and enhanced rainfall over New Guinea, the northeastern portion of Australia and much of the subtropical Pacific at 20°N.

The circulation near the surface (Fig. 14c) is characterized by anomalous easterlies and horizontal divergence along the central equatorial Pacific, as well as by convergence over Indonesia. These circulation changes are accompanied by the intensification of the surface anticyclone over the South Pacific, and lowering of the surface pressure over the western portion of the subtropical North Pacific, Indonesia, Australia and the Indian Ocean (Fig. 14d).

The 200 mb circulation over the tropical Pacific is organized about the pair of elongated cyclones straddling the equator (Figs. 14e and 14f). The wave train spanning the North Pacific–North American sector bears some resemblance to the PNA pattern noted in the previous winter (Figs. 12e and 12f), except that the polarities of the individual cyclonic and anticyclonic centers are reversed. Observational results presented by Horel and Wallace (1981, Fig. 10) suggest a similar sign reversal in the PNA Index after the 1963, 1969 and 1972 El Niños. The pattern in Fig. 14f is also indicative of a weak Southern Hemisphere wave train extending from the tropical Pacific across the southern tip of South America towards the Atlantic.

6. Hovmöller diagrams of simulated anomalies in a typical ENSO episode

In this section the temporal and spatial evolution of various model features in the course of a composite ENSO episode is examined in further detail with the aid of Hovmöller diagrams, which depict the variations of selected parameters at certain fixed latitudes as a function of time and longitude. The ordinate of the diagrams shown here corresponds to the time span from June of year −1 to February of year +2, as defined using the convention adopted in Section 5. The values for a given month along the ordinate represent averages of data for that month over six ENSO episodes. Anomalies are then computed by subtracting from these monthly values the 30-year climatology for the corresponding calendar months. The statistical significance of the anomalous features is ascertained by following the same procedure used in connection with the composite charts, except that Student's t-test is now applied to monthly instead of seasonal values.

In Fig. 15 are shown the Hovmöller diagrams for the monthly anomalies of (a) SST, (b) precipitation, (c) 950 mb zonal wind, (d) 1000 mb height, (e) 200 mb zonal wind and (f) 200 mb height. With the exception of panel (d), these patterns describe the model behavior within the equatorial zone between 4.5°N and 4.5°S. The zone for displaying the 1000 mb height data (Fig. 15d) is chosen to be the latitude belt between 9°S and 18°S. Located within this particular zone are the stations of Darwin (12.4°S, 130.9°E) and Tahiti (17.5°S, 149.6°W), which have been used in constructing the Southern Oscillation Index for sea level pressure presented in Fig. 8. The light, medium and dark shading in Fig. 15 indicate anomalies that exceed the 90, 95 and 99% significance levels, respectively.

The appearance of surface water with above normal temperature off the South American coast and the subsequent spread of the warm anomaly towards the central Pacific in year 0 is delineated in Fig. 15a. Also apparent in this pattern is the evolution of the cold anomaly in year +1.

The precipitation composite in Fig. 15b is characterized by a positive anomaly center extending from 135°W to the date line during the second half of year 0. Dryness is seen to prevail in the Indonesian sector (120°–160°E) through much of the period from the beginning of year 0 to the first half of year +1. In the vicinity of the Line Islands, which lie just north of the Equator between about 155° and 160°W, the simulated precipitation changes are in agreement with the observed temporal evolution of the Precipitation Index for that region as presented by RC (their Fig. 16).

The Hovmöller diagram for zonal wind at 950 mb (Fig. 15c) indicates that the reversal of the anomalous flow over the Pacific Basin from easterlies to westerlies typically takes place in the beginning of year 0. This region comes under the influence of surface easterly anomalies again in the second half of year +1. The zonal wind anomalies over South America and the surrounding waters tend to be directed opposite to the anomalies near the date line. For a given season and a given location, the zonal wind anomaly at 200 mb (Fig. 15e) tends to have a polarity opposite to that of

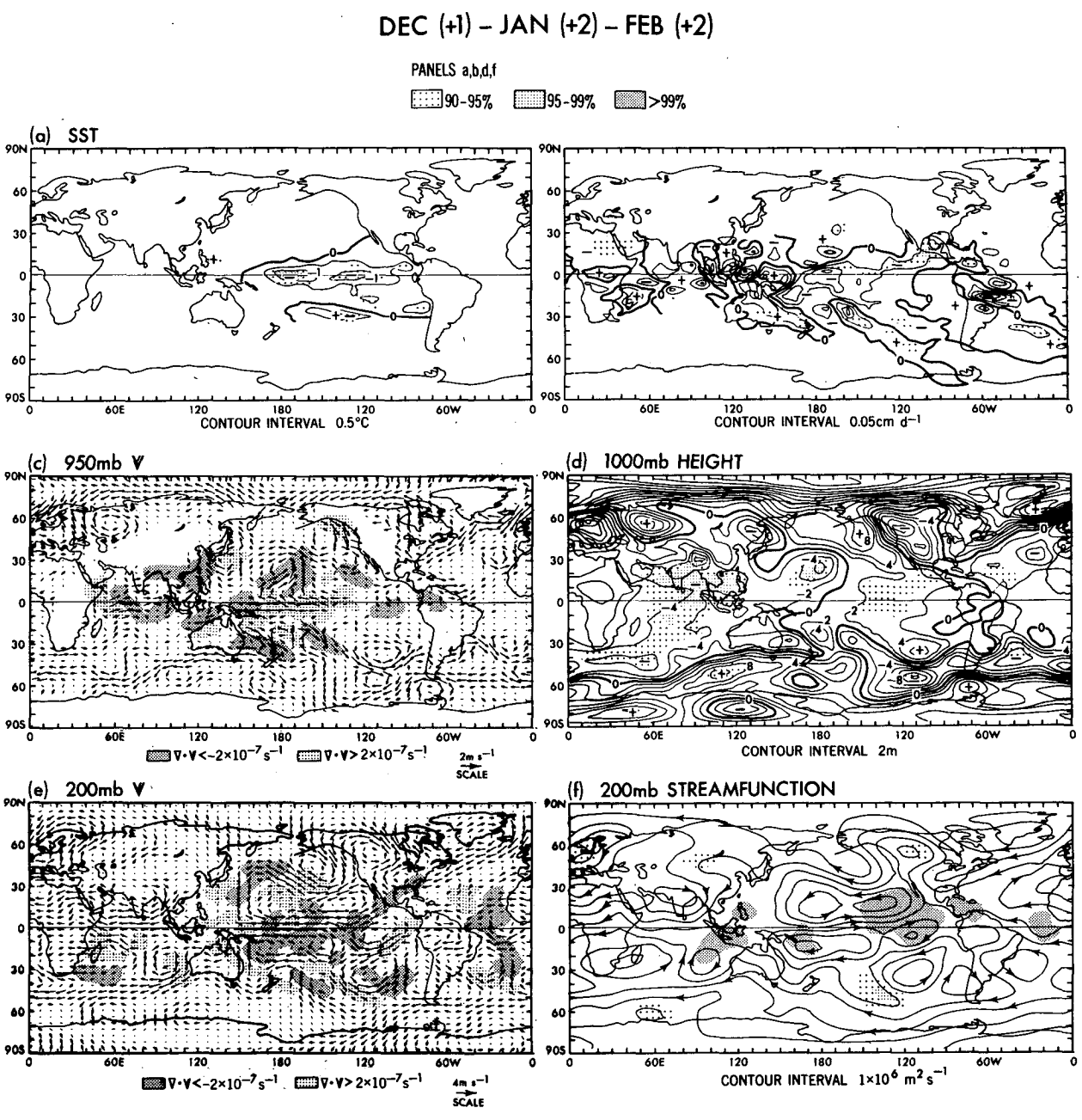

FIG. 14. As in Fig. 9 except for the period of December (+1)–February (+2).

the corresponding anomaly at 950 mb. The most notable feature in the 200 mb diagram is the strong anomalous easterlies near the date line at the end of year 0, and the strong anomalous westerlies over the equatorial Indian and Atlantic Oceans during the same period.

The model results for 1000 mb height (Fig. 15d) indicate that the sea level pressure anomaly over the South Pacific east of the date line changes from positive to negative values near the end of year −1. Above normal pressure returns to this region in the second half of year +1. These model changes are in general agreement with the observed evolution of the sea level pressure anomaly at Tahiti during nine ENSO episodes, as documented by van Loon and Shea (1984, Fig. 4), except that the first observed pressure minimum occurs about two to three months later than is simulated in the model.

The simulated sea level pressure over the western portion of the South Pacific (130°–180°E) remains below or near normal prior to May of year 0, and then attains above normal values through the next 12 months. Below normal pressures prevail again in the second half of year +1. The timing of these simulated

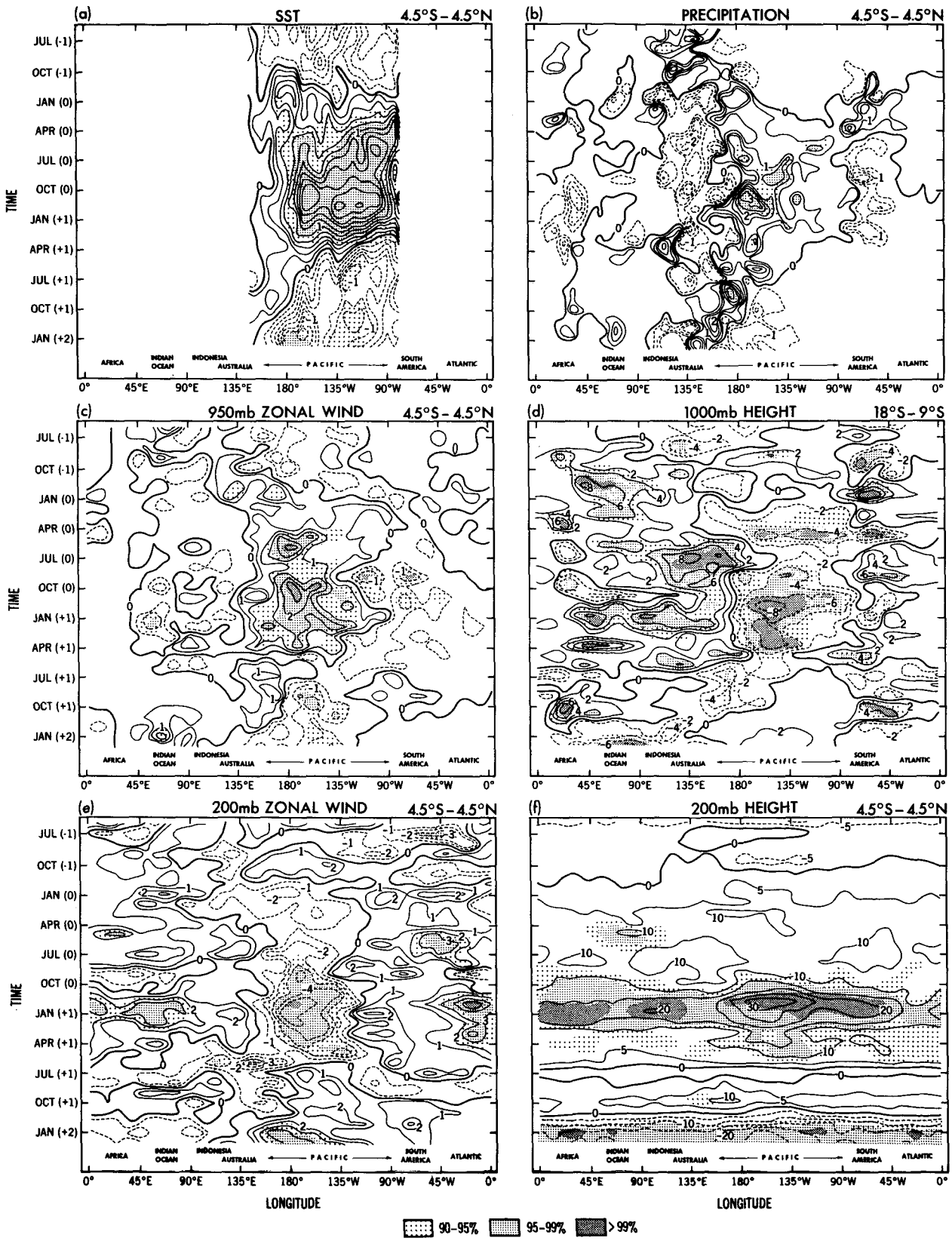

FIG. 15. Distributions of departures from 30-year climatology of (a) sea surface temperature, contour interval 0.2°C, (b) precipitation rate, contour interval 0.05 cm d^{-1}, (c) zonal wind at 950 mb, contour interval 0.5 m s^{-1}, (d) 1000 mb height, contour interval 2 m, (e) zonal wind at 200 mb, contour interval 1 m s^{-1}, and (f) 200 mb height, contour interval 5 m, plotted as functions of longitude and time period in the life cycle of a typical ENSO episode. With the exception of 1000 mb height [panel (d)], spatial averages for the belt extending from 4.5°S to 4.5°N are used. Panel (d) is based on averages for the belt from 18°S to 9°S. All data shown are based on monthly composites of 6 individual ENSO episodes. Light, medium and dark shading indicates anomalies exceeding the 90, 95 and 99% significance levels, respectively, according to Student's t-test.

pressure changes compares favorably with the observational records published by van Loon and Shea (1984, Fig. 4) for Darwin.

Figure 15d suggests that a significant negative anomaly signal is simulated first in the eastern portion of the South Pacific in May of year 0, about two to three months before the arrival of the positive pressure signal in the western portion. This simulated time lag between the opposite ends of the east–west pressure seesaw associated with the Southern Oscillation has been noted in observational studies by Trenberth (1976, Fig. 6), Horel and Wallace (1981) and RC (their Fig. 15).

The most striking feature in the evolution of the simulated 200 mb height at the equator (Fig. 15f) is the zonally symmetric positive anomaly occurring at the end of year 0 and the beginning of year +1. This highly significant response is followed 12 months later by a similar phenomenon with the opposite polarity. The strong seasonal dependence of the pattern in Fig. 15f is consistent with the higher correlation between the SST and 200 mb height indices during Northern Hemisphere winter (Table 1). This model result is substantiated by the data records at various stations located within the equatorial belt, as analyzed by Angell and Korshover (1978), Newell and Weare (1976) and Horel and Wallace (1981). Horel and Wallace have pointed out that since the 200 mb height is a good indicator of the thickness between 1000 and 200 mb in the tropics, and thus of the temperature averaged over the entire tropospheric column, the phenomenon described here implies a uniform warming of the tropical troposphere in the northern winter following the appearance of above normal SST off the South American coasts. However, contrary to the finding reported in the observational study by Pan and Oort (1983), the model results indicate no significant temporal lag between the equatorial SST fluctuations at 130°W and the tropospheric temperature of the tropical belt (cf. Figs. 15a and 15f).

7. Impact of tropical Pacific SST anomalies on atmospheric variability

Manabe and Hahn (1981) and Lau (1981) have analyzed the data from a 15-year integration with a GCM almost identical to that used here but with no interannual SST variability imposed. The previous results from this "unperturbed" experiment (hereafter referred to as the "control" run) hence serve as a convenient yardstick for assessing the impact of tropical Pacific SST fluctuations incorporated in the experiments examined in the present study (hereafter referred to as the "perturbed" runs). In the present discussion, we shall distinguish influences on the tropics from those on the extratropics.

a. Tropical response

It was noted in Lau (1981, Fig. 24b) that no signal of the east–west seesaw in the sea level pressure field over the tropical Pacific and Indian Oceans is detectable in the control run. Manabe and Hahn (1981, Figs. 5.6 and 5.7) have further pointed out that the standard deviations of monthly averaged 1000 mb heights in the tropics of the control experiment are considerably lower than the observed values. On the other hand, it is demonstrated in the present study that a prominent signature of the Southern Oscillation is present in the composites when SST anomalies are introduced in the tropical Pacific. As was done in Lau (1981), the 1000 mb height data from the perturbed runs examined here have also been analyzed using empirical orthogonal functions. The results reveal that one of the principal modes of variability (not shown) is characterized by an east–west dipole pattern resembling the composite charts displayed here (e.g., see Fig. 12d) and the teleconnection chart presented in Lau and Oort (1985, Fig. 2b).

The incremental variance of 1000 mb height attributable to SST variability in the tropical Pacific is portrayed in Fig. 16a, which shows the ratio of the variance of monthly averaged 1000 mb height in the perturbed experiments to the corresponding quantity in the control run. Only data for the months of December, January and February are used in the computations. The variance for the control run is based on history tapes for 10 years of the 17.75-year simulation. The variance for the perturbed runs is based on records for the entire 30-year period. As a crude indicator of the statistical significance of the ratios mapped in Fig. 16, we note here that, according to the *F*-Tables (Panofsky and Brier, 1958), the variances for the perturbed run would be larger than that for the control run at the 95% confidence level if the ratio in question is larger than 1.95. The above test is conducted with the assumption that each 3-month season has two independent data samples, so that the numbers of degrees of freedom in the estimation of the variance quantities in the numerator and denominator of the ratio considered here are approximately 60 and 20, respectively. Inspection of the pattern in Fig. 16a reveals that the ratio is larger than unity over a large fraction of the tropics, with significant maxima over the Indonesian Archipelago, the eastern tropical Pacific, and portions of the Indian Ocean lying west of Australia. These centers of enhanced variability share approximately the same locations with the principal 1000 mb height anomalies appearing in the composite charts shown in Section 5.

In the upper troposphere, Lau (1981, Fig. 24a) has indicated that the dominant mode of variability in the 300 mb height field over the tropics of the control run exhibits a zonally symmetric pattern, with maximum amplitude near the equator. Whereas this mode bears a considerable resemblance to the model response at 200 mb near the end of year 0 in the perturbed runs (see Fig. 15f), the standard deviations of monthly mean geopotential heights in the tropical upper atmosphere of the control run were found to be less than the observed values by a factor of 2–3 (see Manabe and Hahn,

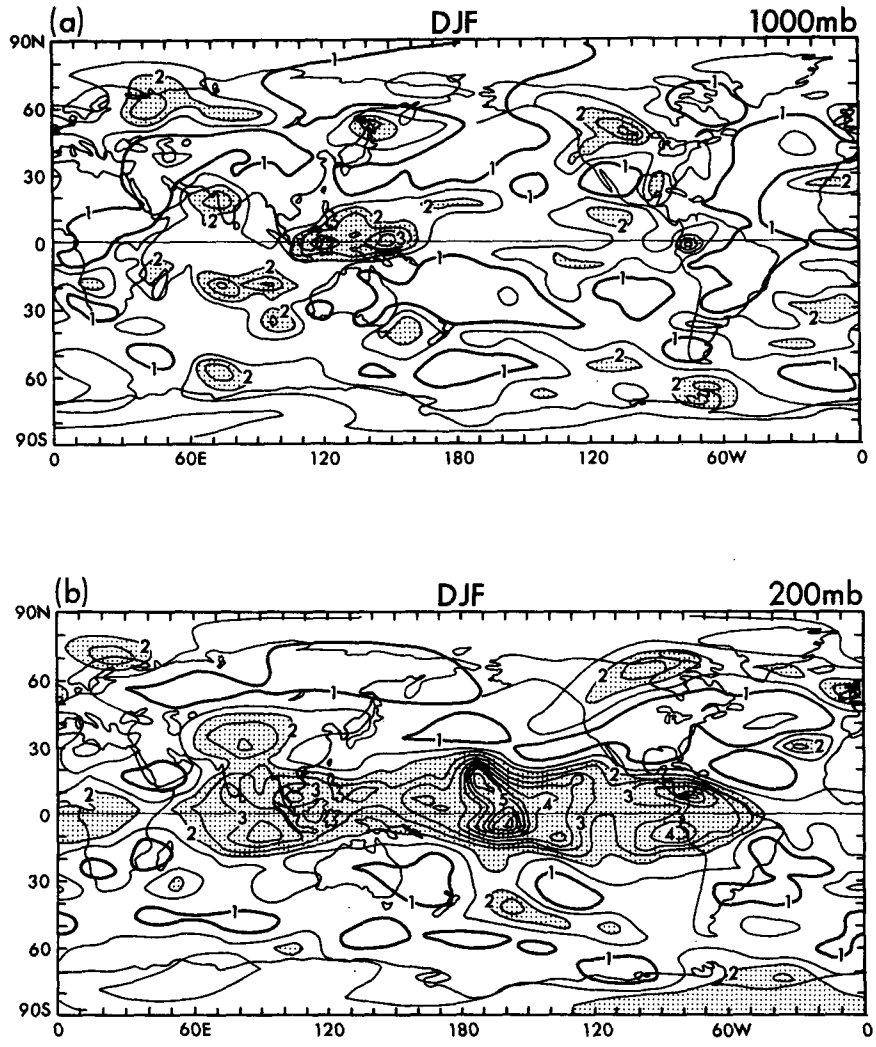

FIG. 16. Distributions of the ratio of variances of geopotential heights at (a) 1000 mb and (b) 200 mb in the perturbed experiment to the corresponding values in the control experiment, as computed using the monthly means for December–February. Contour interval 0.5. Thick contours correspond to ratios equal to 1. Shading indicates values larger than 2.

1981, Fig. 5). The extent to which this model deficiency is remedied by the imposition of SST anomalies may be inferred from Fig. 16b, in which the ratio of the variances of 200 mb height in the perturbed and control runs is mapped. It is seen that the variance within almost the entire tropical belt in the perturbed run is substantially higher than that in the control run, with the ratio attaining values as large as 4–6 over the central equatorial Pacific.

In summary, the collective findings based on the control and perturbed GCM experiments are indicative of the importance of SST fluctuations in determining both the amplitude and characteristic spatial pattern of interannual variability in the tropical atmosphere. Influences of SST conditions on the spatial structure are most marked near the surface, whereas amplitude enhancement is strongest in the upper troposphere.

b. Extratropical response

The variance statistics presented by Manabe and Hahn (1981, Figs. 5.6–5.10) indicate that the "natural" variability in the extratropics of the control experiment is already comparable with the observed values. Lau (1981, Figs. 5–10) provided further evidence that, even in the absence of variable SST forcing, the model atmosphere exhibits recurrent meteorological anomalies which resemble the PNA pattern in many respects. This characteristic pattern accounts for only about 20–25% of the spatially integrated variance of the extratropical 500 and 1000 mb height fields in both the control and perturbed experiments. The fraction of the variance associated with the PNA pattern that is in turn attributable to SST variations in the tropical Pacific, as estimated by squaring the wintertime values in the last

two columns of Table 1 in the present paper, is also found to be quite small (less than 30%). It hence appears that the impact of equatorial Pacific SST anomalies on the circulation in the extratropics is considerably weaker than in the tropics, and that physical and dynamical processes in addition to those directly associated with SST anomalies may also be linked to the occurrence of the PNA pattern. These notions are reinforced by the ratios of variances displayed in Figs. 16a and 16b. It is seen that this ratio does not differ significantly from unity in most of the extratropical zones, with the possible exception of northern and western Canada. In particular, the patterns in Fig. 16 indicate no significant amplitude enhancement of the variability in the perturbed runs over the central North Pacific and the southeastern United States, which correspond to two of the three extratropical centers of action associated with the PNA pattern.

8. Concluding Remarks

The primary objective for constructing the composite charts in Sections 5 and 6 is to delineate those aspects of the model response that are common to different ENSO episodes. That such a composite approach is meaningful for much of the warm phase (year 0) and the peak of the cold phase (end of year +1) is affirmed by the high significance levels of the model features appearing in these periods. On the other hand, it is noteworthy that much weaker statistical significance is obtained for simulated anomalies occurring in year −1 and the beginning of year 0, which correspond to the period prior to the onset of the warm phase (Fig. 15). One of the contributing factors to the relatively feeble signals in this period could be the occurrence of a pronounced positive SST anomaly in the central equatorial Pacific in 1968 (Fig. 2), which is classified as "year −1" in the present composite scheme, since it happens to precede the 1969 El Niño. The composite phenomena in year −1 must hence be interpreted with some caution.

Difficulties encountered in applying the composite procedure, such as those pertaining to the 1968/69 event mentioned before, suggest that it is equally important to investigate the differences between individual El Niño events. History tapes for the pair of 15-year integrations examined here, which can provide only two model realizations for each El Niño, are probably insufficient for studying the steady model response to individual anomalous SST episodes. A detailed investigation of the variability among different ENSO cycles would therefore entail several additional long-term integrations similar to those described here, and preferably with an even more extended duration so as to incorporate the unusual 1976/77 and 1982/83 events.

In comparing the model results with observations, it is necessary to bear in mind that the observed atmospheric anomalies represent the net response to a variety of internal and external forcing mechanisms in the global climate system, of which sea–air interaction over the tropical Pacific is just one particular component. Since Pan and Oort (1983, Fig. 8b) have shown that SST fluctuations in the equatorial Pacific are positively correlated with SST changes in the tropical Atlantic and Indian Oceans, some of the observed ENSO phenomena might be responding to SST anomalies present in the latter regions. The discrepancies between model and observations could hence be partially accounted for by the absence of SST variability outside the tropical Pacific in the model integrations. The extent to which these discrepancies may be remedied by imposing SST changes everywhere in the World Oceans, and by incorporating more realistic model physics (such as a fully interactive cloud parameterization), remains to be ascertained by actual experimentation.

In another diagnostic work using complex eigenvectors, Barnett (1985) has described the Southern Oscillation as part of a global-scale propagating mode in sea level pressure. By applying the same analysis tool to the present GCM simulation, he further demonstrated that, whereas the model is capable of reproducing the opposing pressure changes over the South Pacific and the Indonesia–Australian sector, it does not exhibit some of the propagation characteristics seen in the observations. Hence the relationship between the global signal revealed in Barnett's study and various forcing mechanisms requires further study.

A qualitative approach has been adopted in the present paper in describing various phenomena associated with ENSO. In order to identify the nature of various processes operating in the ENSO cycle, and to interpret the differences in model response during individual episodes, more incisive diagnoses of the model data are evidently called for. In view of the complex array of highly interactive processes incorporated in a GCM, diagnostic studies based on model history tapes alone might not be adequate for achieving a thorough understanding of the simulated phenomena. Such analysis needs to be supplemented by experiments with a hierachy of simplified mechanistic models aimed at dissecting the interrelationships among the thermal, dynamical and hydrological components of the climate system in different stages of development during an ENSO episode.

The primary objective of the perturbed runs is to demonstrate that, given a set of realistic conditions at the air–sea interface which are evolving both in space and in time, and in the presence of the seasonal cycle, the current generation of GCMs is able to simulate various facets of the atmospheric response with an acceptable degree of fidelity. Since the model atmosphere does not exert any influence on the oceanic conditions in the present experiment, a full understanding of the underlying causes for the onset, maintenance and breakdown of the SST anomalies themselves is beyond

the scope of this study. An attempt at such an understanding must await the diagnosis of extended integrations with fully interactive ocean–atmosphere coupled models. However, the results presented in the preceding sections indicate that, once the warm and cold SST anomalies are established and spread across the equatorial Pacific, the GCM is capable of simulating meteorological features which are in reasonable agreement with observations in such aspects as amplitude, spatial pattern and seasonal dependence. The present simulation, in conjunction with the success reported by Philander and Seigel (1985) of ocean GCMs in generating realistic anomalies when subjected to prescribed changes in the wind stress at the upper boundary, offer encouraging signs that coupled atmospheric–ocean models might eventually be an effective tool in comprehending the full realm of natural phenomena associated with ENSO.

Acknowledgments. I am indebted to S. Manabe for the opportunity of using the GCM designed by the Climate Dynamics Project at GFDL. I have benefited from several conversations with J. Shukla in the design stage of this study. E. Rasmusson and T. Carpenter have been cooperative in supplying the SST dataset compiled at CAC. D. Daniel and D. Hahn have offered me programming support when the actual numerical integrations were performed. I also wish to thank P. Arkin, T. Barnett, I. Held, S. Manabe, A. Oort, G. Philander, E. Pitcher, K. Trenberth, H. van Loon and J. M. Wallace for reading the manuscript and for offering insightful comments. The figures were prepared by the GFDL Scientific Illustration Group and J. Conner. Several drafts of the manuscript were typed by J. Kennedy.

REFERENCES

Angell, J. K., and J. Korshover, 1978: Estimates of global temperature variations in the 100–30 mb layer between 1958 and 1977. *Mon. Wea. Rev.*, **106,** 1422–1432.

Arkin, P. A., 1982: The relationship between interannual variability in the 200 mb tropical wind field and the Southern Oscillation. *Mon. Wea. Rev.*, **110,** 1393–1404.

Barnett, T. P., 1985: Variations in near-global sea level pressure. *J. Atmos. Sci.*, **42,** 478–501.

Bjerknes, J., 1966: A possible response of the atmospheric Hadley circulation to equatorial anomalies of ocean temperature. *Tellus,* **18,** 820–829.

——, 1969: Atmospheric teleconnections from the equatorial Pacific. *Mon. Wea. Rev.*, **97,** 163–172.

Blackmon, M. L., J. E. Geisler and E. J. Pitcher, 1983: A general circulation model study of January climate anomaly patterns associated with interannual variation of equatorial Pacific sea surface temperatures. *J. Atmos. Sci.*, **40,** 1410–1425.

Boer, G. J., 1985: Modelling the atmospheric response to the 1982/83 El Niño. *Proc. 16th Int. Liége Colloquium on Ocean Hydrodynamics.* Chap. 2, Elsevier Oceanography Series, 767 pp.

Chen, W. Y., 1982a: Assessment of Southern Oscillation sea-level pressure indices. *Mon. Wea. Rev.*, **110,** 800–807.

——, 1982b: Fluctuations in Northern Hemisphere 700 mb height field associated with the Southern Oscillation. *Mon. Wea. Rev.*, **110,** 808–823.

Chervin, R. M., and S. H. Schneider, 1976: On determining the statistical significance of climate experiments with general circulation models. *J. Atmos. Sci.*, **33,** 405–412.

Dorman, C. E., and R. H. Bourke, 1979: Precipitation over the Pacific Ocean, 30°S to 60°N. *Mon. Wea. Rev.*, **107,** 896–910.

——, and ——, 1981: Precipitation over the Atlantic Ocean, 30°S to 70°N. *Mon. Wea. Rev.*, **109,** 554–563.

Heddinghaus, T. R., and A. F. Krueger, 1981: Annual and interannual variations in outgoing longwave radiation over the tropics. *Mon. Wea. Rev.*, **109,** 1208–1218.

Horel, J. D., 1982: On the annual cycle of the tropical Pacific atmosphere and ocean. *Mon. Wea. Rev.*, **110,** 1863–1878.

——, and J. M. Wallace, 1981: Planetary scale atmospheric phenomena associated with the Southern Oscillation. *Mon. Wea. Rev.*, **109,** 813–829.

Julian, P. R., and R. M. Chervin, 1978: A study of the Southern Oscillation and Walker Circulation phenomenon. *Mon. Wea. Rev.*, **106,** 1433–1451.

Keshavamurty, R. N., 1982: Response of the atmosphere to sea surface temperature anomalies over the equatorial Pacific and the teleconnections of the Southern Oscillation. *J. Atmos. Sci.*, **39,** 1241–1259.

Krishnamurti, T. N., 1971: Tropical east–west circulations during the northern summer. *J. Atmos. Sci.*, **28,** 1342–1347.

——, M. Kanamitsu, W. J. Koss and J. D. Lee, 1973: Tropical east–west circulations during the northern winter. *J. Atmos. Sci.*, **30,** 780–787.

Krueger, A. F., and T. I. Gray, Jr., 1969: Long-term variations in equatorial circulation and rainfall. *Mon. Wea. Rev.*, **97,** 700–711.

Lau, K-M., and P. H. Chan, 1983: Short-term climate variability and atmospheric teleconnections from satellite-observed outgoing longwave radiation. Part I: Simultaneous relationships. *J. Atmos. Sci.*, **40,** 2735–2750.

Lau, N-C., 1981: A diagnostic study of recurrent meteorological anomalies appearing in a 15-year simulation with a GFDL general circulation model. *Mon. Wea. Rev.*, **109,** 2287–2311.

——, 1984a: Circulation statistics based on FGGE Level III-B analyses produced by GFDL. NOAA Data Rep. ERL GFDL-5, 429 pp. [Available from GFDL, P.O. Box 308, Princeton, NJ 08542].

——, 1984b: A comparison of circulation statistics based on FGGE Level III-B analyses produced by GFDL and ECMWF for the special observing periods. NOAA Data Rep. ERL GFDL-6, 237 pp. [Available from GFDL, P.O. Box 308, Princeton, NJ 08542].

——, and A. H. Oort, 1985: Response of a GFDL general circulation model to SST fluctuations observed in the tropical Pacific Ocean during the period 1962–1976. *Proc. 16th Int. Liège Colloquium on Ocean Hydrodynamics.* Elsevier Oceanography Series, 767 pp.

Manabe, S., and D. G. Hahn, 1981: Simulation of atmospheric variability. *Mon. Wea. Rev.*, **109,** 2260–2286.

——, and J. L. Holloway, Jr., 1975: The seasonal variation of the hydrologic cycle as simulated by a global model of the atmosphere. *J. Geophys. Res.*, **80,** 1617–1649.

——, D. G. Hahn and J. L. Holloway, Jr., 1979: Climate simulations with GFDL spectral models of the atmosphere: Effect of spectral truncation. *GARP Publ. Ser. No. 22,* Vol. 1, 41–94. [NTIS N8027917].

Michaud, R., and R. Sadourny, 1984: Numerical simulation of the atmospheric response to a composite January El Niño anomaly. *Trop. Ocean-Atmos. Newslett.*, No. 27, 5–6.

Mo, K. C., and G. H. White, 1985: Teleconnections in the Southern Hemisphere. *Mon. Wea. Rev.*, **113,** 22–37.

Newell, R. E., and B. C. Weare, 1976: Ocean temperatures and large scale atmospheric variations. *Nature,* **262,** 40–41.

Oort, A. H., 1983: Global Atmospheric Circulation Statistics, 1958–1973. NOAA Prof. Paper No. *14,* U.S. Government Printing Office, Washington, DC 20402, 180 pp. + 47 microfiches [NTIS PB8 4 129717].

Palmer, T. N., and D. A. Mansfield, 1984: Response of two atmospheric general circulation models to sea-surface temperature

anomalies in the tropical east and west Pacific. *Nature,* **310,** 483–485.

Pan, Y. H., and A. H. Oort, 1983: Global climate variations connected with sea surface temperature anomalies in the eastern equatorial Pacific Ocean for the 1958–73 period. *Mon. Wea. Rev.,* **111,** 1244–1258.

Panofsky, H. A., and G. W. Brier, 1958: *Some Applications of Statistics to Meteorology.* The Pennsylvania State University, University Park, PA, 16802, 224 pp.

Philander, S. G. H., 1983: El Niño–Southern Oscillation phenomena. *Nature,* **302,** 295–301.

——, and A. D. Seigel, 1985: Simulation of El Niño of 1982–1983: *Proc. of the 16th Int. Liége Colloquium on Ocean Hydrodynamics.* Chap. 33, Elseiver Oceanography Series, 767 pp.

Ramage, C. S., 1975: Preliminary discussion of the meteorology of the 1972/73 El Niño. *Bull. Amer. Meteor. Soc.,* **56,** 234–242.

Rasmusson, E. M., and T. H. Carpenter, 1982: Variations in tropical sea surface temperature and surface wind fields associated with the Southern Oscillation/El Niño. *Mon. Wea. Rev.,* **110,** 354–384.

——, and T. H. Carpenter, 1983: The relationship between eastern equatorial Pacific sea surface temperatures and rainfall over India and Sri Lanka. *Mon. Wea. Rev.,* **111,** 517–528.

——, and J. M. Wallace, 1983: Meteorological aspects of the El Niño/Southern Oscillation. *Science,* **222,** 1195–1202.

Rogers, J. C., 1984: The association between the North Atlantic Oscillation and the Southern Oscillation in the Northern Hemisphere. *Mon. Wea. Rev.,* **112,** 1999–2015.

Sardeshmukh, P. D., and B. J. Hoskins, 1985: Vorticity balances in the tropics during the 1982/83 El Niño–Southern Oscillation event. *Quart. J. Roy. Meteor. Soc.,* **111,** 261–278.

Shukla, J., and D. A. Paolino, 1983: The Southern Oscillation and long-range forecasting of the summer monsoon rainfall over India. *Mon. Wea. Rev.,* **111,** 1830–1837.

——, and J. M. Wallace, 1983: Numerical simulation of the atmospheric response to equatorial Pacific sea surface temperature anomalies. *J. Atmos. Sci.,* **40,** 1613–1630.

Trenberth, K. E., 1976: Spatial and temporal variations in the Southern Oscillation. *Quart. J. Roy. Meteor. Soc.,* **102,** 639–653.

——, 1980: Planetary waves at 500 mb in the Southern Hemisphere. *Mon. Wea. Rev.,* **108,** 1378–1389.

——, 1981: Observed Southern Hemisphere eddy statistics at 500 mb: Frequency and spatial dependence. *J. Atmos. Sci.,* **38,** 2585–2605.

——, and D. A. Paolino, 1981: Characteristic patterns of variability of sea level pressure in the Northern Hemisphere. *Mon. Wea. Rev.,* **109,** 1169–1189.

van Loon, H., and R. A. Madden, 1981: The Southern Oscillation. Part I: Global associations with pressure and temperature in northern winter. *Mon. Wea. Rev.,* **109,** 1150–1162.

——, and J. C. Rogers, 1981: The Southern Oscillation. Part II: Associations with changes in the middle troposphere in northern winter. *Mon. Wea. Rev.,* **109,** 1163–1168.

——, and D. J. Shea, 1984: The origin of a warm event in the Southern Oscillation. *Trop. Ocean-Atmos. Newslett.,* No. 27, 1–2.

Walker, G. T., and E. W. Bliss, 1932: World Weather V. *Mem. Roy. Meteor. Soc.,* **4,** 53–84.

Wallace, J. M., 1983: The climatological mean stationary waves: Observational evidence. *Large-Scale Dynamical Processes in the Atmosphere,* B. J. Hoskins and R. P. Pearce, Eds. Academic Press, 27–53.

——, and D. S. Gutzler, 1981: Teleconnections in the geopotential height field during the Northern Hemisphere winter. *Mon. Wea. Rev.,* **109,** 784–812.

White, G. H., 1982: An observational study of the Northern Hemisphere extratropical summertime general circulation. *J. Atmos. Sci.,* **39,** 24–40.

Wright, P. B., 1977: The Southern Oscillation—patterns and mechanisms of the teleconnections and the persistence. Hawaii Inst. Geophys. Rep. HIG-77-13, University of Hawaii, Honolulu, Hawaii 96822, 107 pp.

Wyrtki, K., and G. Meyers, 1976: The trade wind field over the Pacific Ocean. *J. Appl. Meteor.,* **15,** 698–704.